Spring 2015

Computational optical imaging: Applications in synthetic aperture imaging, phase retrieval, and digital holography

Dennis Joseph Lee
Purdue University

Graduate School Form 30
(Revised 08/14)

PURDUE UNIVERSITY
GRADUATE SCHOOL
Thesis/Dissertation Acceptance

This is to certify that the thesis/dissertation prepared

By Dennis Joseph Lee

Entitled
Computational Optical Imaging: Applications in Synthetic Aperture Imaging, Phase Retrieval, and Digital Holography

For the degree of Doctor of Philosophy

Is approved by the final examining committee:

ANDREW M. WEINER

CHARLES A. BOUMAN

DAN JIAO

JAMES V. KROGMEIER

To the best of my knowledge and as understood by the student in the Thesis/Dissertation Agreement, Publication Delay, and Certification/Disclaimer (Graduate School Form 32), this thesis/dissertation adheres to the provisions of Purdue University's "Policy on Integrity in Research" and the use of copyrighted material.

ANDREW M. WEINER

Approved by Major Professor(s): _____

Approved by: Michael R. Melloch 04/21/2015

Head of the Department Graduate Program Date

COMPUTATIONAL OPTICAL IMAGING: APPLICATIONS IN SYNTHETIC APERTURE IMAGING, PHASE RETRIEVAL, AND DIGITAL HOLOGRAPHY

A Dissertation

Submitted to the Faculty

of

Purdue University

by

Dennis Joseph Lee

In Partial Fulfillment of the

Requirements for the Degree

of

Doctor of Philosophy

May 2015

Purdue University

West Lafayette, Indiana

To my family

ACKNOWLEDGMENTS

I would like to thank my advisor Professor Andrew M. Weiner for his guidance and support during my graduate studies. It has been a great pleasure to work with him and receive his feedback as I performed independent research. I would like to thank Dr. Daniel E. Leaird for his invaluable technical support. I would like to thank Professor Charles Bouman for numerous helpful discussions. Much of the work in Chapter 4 is inspired by his ideas on model based image processing. I would like to thank Professor Dan Jiao and Professor James Krogmeier for their advice and encouragement and for serving on my committee.

I would like to thank my colleagues and classmates Kyunghun Han for sharing his cleanroom expertise to fabricate the grating samples used in Chapters 3 and 4, Hyeon Jeong Lee for helping with cell sample preparation, Professor Juliet Gopinath and Ramzi Zahreddine for numerous discussions about electrically tunable lenses; Professor Ji-Xin Cheng, Professor Victor Torres-Company, Dr. Hyoung-Jun Kim, Yihan Li, Bohao Liu, Jingjing Liu, Yang Liu, Joseph Lukens, A. J. Metcalf, Justus Ndukaife, Professor Minghao Qi, Amir Rashidinejad, Mikhail Shalaginov, Dr. Jian Wang, Pei-Hsun Wang, Dr. Ping Wang, and Dr. Delong Zhang for helpful discussions. I would like to thank the faculty and staff of the School of ECE at Purdue University for welcoming me as a graduate student. Finally I would like to thank my family for their love and support.

TABLE OF CONTENTS

Page

Page

LIST OF TABLES

LIST OF FIGURES

Figure Page

ABSTRACT

Lee, Dennis Joseph Ph.D., Purdue University, May 2015. Computational Optical Imaging: Applications in Synthetic Aperture Imaging, Phase Retrieval, and Digital Holography. Major Professor: Andrew M. Weiner.

Computational imaging has become an important field, as a merger of both algorithms and physical experiments. In the realm of microscopy and optical imaging, an important application is the problem of improving resolution, which is bounded by wavelength and numerical aperture according to the classic diffraction limit. We will investigate the resolution enhancement of phase objects such as transparent biological cells. One key challenge is how to measure phase experimentally. Standard interferometric techniques have the drawback of being sensitive to environmental vibrations and temperature fluctuations, and they use a reference arm which requires more space and cost. Non-holographic methods provide a way to overcome these disadvantages. Another challenge is how to reconstruct phase and amplitude from a digital hologram. The typical method of applying a filter in the frequency domain is limited by finite filter size. Optimization approaches offer a solution to this problem.

The work presented here spans three main aspects of phase imaging microscopy including synthetic aperture imaging, phase retrieval, and digital holography. We develop a non-holographic microscope that uses off-axis illumination for resolution enhancement and demonstrate the first experimental measurements of referenceless phase retrieval at multiple angles. We implement a synthetic aperture microscope using an electrically tunable lens to defocus images, which avoids the need to mechanically move a camera on a translation stage. Finally, we improve the reconstruction of images from a digital hologram based on an iterative algorithm that alternatively updates amplitude and phase.

1. INTRODUCTION

Much of our research focuses on a classic imaging problem: how can we surpass the diffraction limit? Physically, this limit arises from the finite aperture of the objective. When light strikes a sample, higher orders of diffraction will miss the lens aperture as depicted in Fig. 1.1. The numerical aperture (NA) of a lens quantifies how much light is collected. It is defined as NA $= n \sin\theta$, where n is the refractive index of the medium between sample and lens, and θ is the half angle of the maximum cone of light that can enter the lens. According to Abbe's diffraction limit, resolution is roughly λ/NA. Correspondingly, the highest spatial frequency that can be captured by a lens is about NA/λ. In many practical imaging systems, wavelength is fixed or too difficult to change. Numerical aperture is practically bounded at 1.4; there are challenges in manufacturing larger NA objectives.

If λ and NA are practically fixed or bounded, are there other ways to increase resolution? Various techniques have been proposed over the years [1], and we will mention a few in passing. Confocal microscopy relies on a spatial pinhole placed at

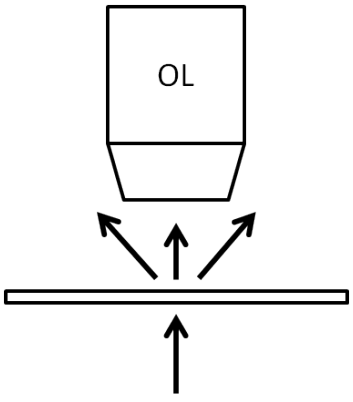

Fig. 1.1. The objective lens (OL) captures some spatial frequencies but misses others.

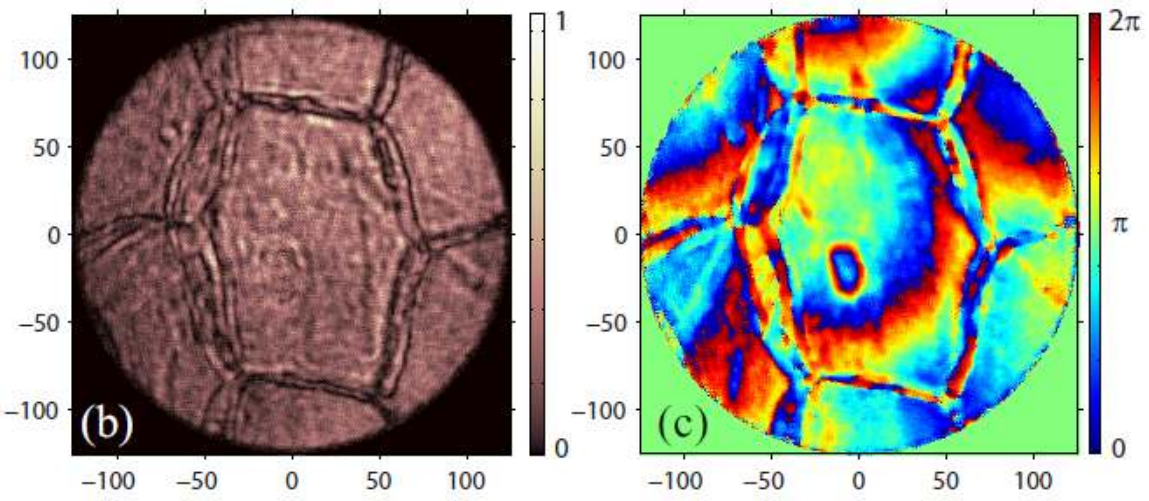

Fig. 1.2. Example of intensity (left) and phase (right) images of an onion skin cell. The phase image reveals cellular structure such as the nucleus. Adapted from [2].

the confocal plane of the lens to eliminate out-of-focus light. 4π microscopy uses two opposing objectives for excitation and detection. Structured illumination microscopy applies patterned illumination to the sample, shifting higher frequencies into the lens.

These techniques are well-known, and they work well for fluorescent samples. However, not all samples are easily fluorescently tagged. We will consider phase objects such as transparent biological cells. Fortunately, transparent samples have an important property that we can exploit for visualization, namely the refractive index contrast between the sample and background. This index contrast gives rise to a path length difference. By imaging phase, or path length differences, we can visualize transparent samples as shown in Fig. 1.2. In addition, amplitude and phase comprise an electric field, which can be numerically propagated to adjust focus on a computer [3, 4].

Our goal is to enhance the resolution of these phase images. A common technique is to use off-axis illumination. By illuminating the sample at multiple angles, different orders of diffraction and spatial frequencies can be captured as illustrated in Fig.

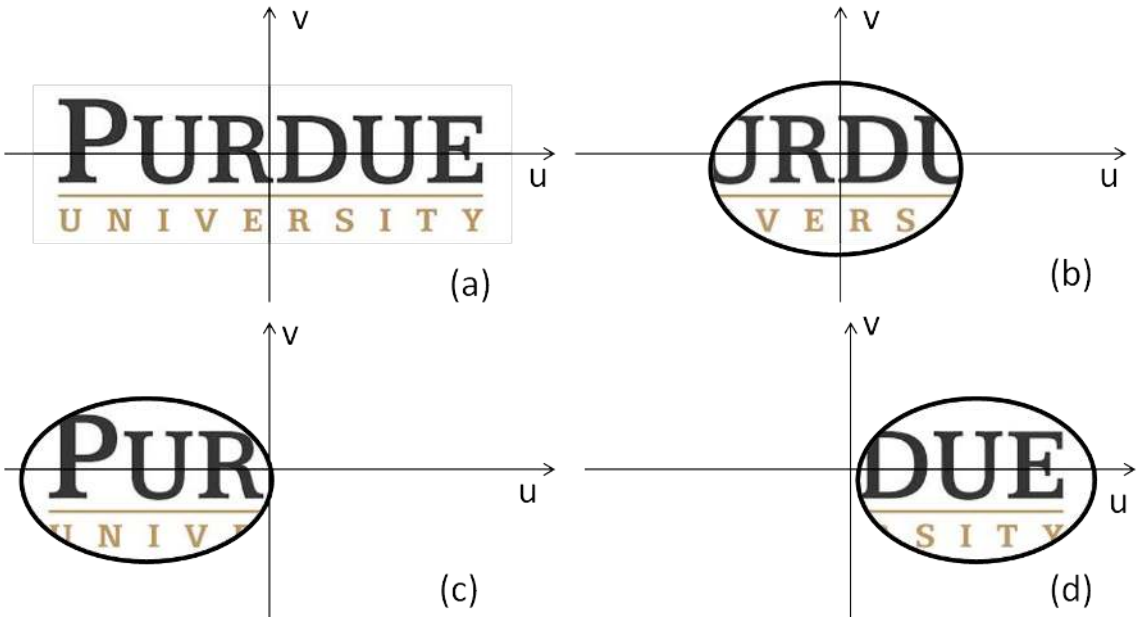

Fig. 1.3. Illustration of synthetic aperture imaging. (a) Original spectrum. (b) Passband centered at DC. (c) Passband with oblique illumination 1. (d) Passband with oblique illumination 2.

1.3. Synthetic aperture imaging combines the images measured over all the angles to obtain an enhanced image. Experimentally, a standard way of measuring the complex electric field is to use holography, a form of interferometry. Holography is commonly used, but it does have its drawbacks. The interferometric configuration is subject to environmental vibrations and temperature fluctuations. Phase-shifting interferometry requires extra parts such as a high frame rate camera. These drawbacks motivate us to develop algorithms and experiments to measure phase in a referenceless, non-interferometric manner.

In addition to solving phase retrieval problems non-interferometrically, this dissertation also tackles problems in digital holography. A classic problem is to extract amplitude and phase from an interference pattern, or hologram, measured on a camera. A standard solution is to take the Fourier transform of the interference pattern and apply a filter in the frequency domain. However, this approach is limited by the finite filter window size, which may cut off higher frequencies. This drawback motivates us to extend some of the techniques in the current literature to improve image reconstruction from a measured hologram.

The unifying theme of this dissertation is computational imaging, a field that is a merger of algorithms and experiment. In particular, the application of phase imaging microscopy relies on various algorithms to form images of transparent samples from raw camera data. This dissertation covers numerous aspects of phase imaging microscopy including synthetic aperture imaging, phase retrieval, and digital holography.

1.1 Organization of the Dissertation with Summary of our Contributions

Imaging phase objects such as transparent biological cells is an important application in microscopy. In Chapter 2, we develop a microscope for enhancing the resolution of phase objects. The developed microscope measures phase in a referenceless, non-holographic manner. This approach avoids interferometric issues with

stability due to environmental vibrations or temperature fluctuations, and it reduces the expense and number of parts needed since a reference arm is not required. Experiments are carried out to test the proposed method. To verify phase measurements and demonstrate resolution enhancement, we image 10 μm polystyrene beads. We apply an iterative phase retrieval algorithm to compute phase at each angle, and we formulate a procedure to combine the angular electric field images to form a synthesized enhanced image. The resulting phase shows a 56% reduction in background noise with 11 total angles. To quantify resolution enhancement, we image particles on a glass slide. The estimated resolution with on-axis illumination is 1.59 μm. After synthetic aperture imaging, the resolution improves to 1.24 μm, verifying our technique.

In Chapter 3, we extend the idea of synthetic aperture microscopy based on referenceless phase retrieval. A slight drawback of our earlier implementation is that it requires a mechanical translation stage to physically move the CCD camera for defocusing images. To eliminate this mechanical motion, we propose to defocus images by changing the focal length of an electrically tunable lens (ETL), a relatively compact and inexpensive device compared to the translation stage. We develop a calibration algorithm to correct for image shifts and magnifications that may occur as the ETL changes focal length. We fabricate a 1 μm grating on PMMA film to demonstrate resolution enhancement. Based on phase measurements of our grating, we are able to see sub-μm resolution, with an increase in NA to 0.97 from 0.75. Finally we apply our techinique to imaging biological cells. Using our ETL-based setup for synthetic aperture imaging, we are able to observe enhanced features in the cell compared to using only on-axis illumination.

Besides phase retrieval, digital holography is a common way to characterize the amplitude and phase of a sample, and it is used in many applications including microscopy, 3D displays, and THz imaging. In Chapter 4, we propose an iterative algorithm to further improve the reconstruction of images from a digital hologram. The standard method is based on applying a filter in the frequency domain, but this

approach is limited by the finite filter window size. More recent literature frames digital holography as an inverse problem, based on minimizing cost as a function of the complex object field. We propose a novel way of minimizing cost based on updating the amplitude and phase separately. Our technique offers an improvement over current algorithms because prior knowledge such as object smoothness can be applied to amplitude and phase separately, and it doesn't require phase unwrapping. Also, since low amplitudes multiply phase as $u = Ae^{i\phi}$, updating phase separately helps to decouple the effects of poor SNR on phase. We demonstrate the effectiveness of our algorithm on simulated and experimental data. From our results, we see that our technique can reconstruct higher quality images with better resolution and less artifacts than standard Fourier filtering.

Finally in Chapter 5, we summarize our work and present possible future research directions.

2. OPTICAL PHASE IMAGING USING A SYNTHETIC APERTURE PHASE RETRIEVAL TECHNIQUE

Optical phase imaging enables visualization of transparent samples, numerical refocusing, and other computational processing. Typically phase is measured quantitatively using interferometric techniques such as digital holography. Researchers have demonstrated image enhancement by synthetic aperture imaging based on digital holography. In this work we introduce a novel imaging technique that implements synthetic aperture imaging using phase retrieval, a non-interferometric technique. Unlike digital holography, phase retrieval obviates the need for a reference arm and provides a more compact, less expensive, and more stable experimental setup. We call this technique synthetic aperture phase retrieval.

2.1 Introduction

2.1.1 Measuring Phase

Optical phase imaging finds important applications in biomedical imaging where samples are often transparent and weakly scattering. Phase contains valuable information such as refractive index variations or sample thickness that intensity alone cannot provide [5–7]. Quantitative knowledge of phase, combined with intensity measurements, yields the complex field. The field is a powerful computational tool because it allows the sample to be post-processed after experimental measurements are taken. For example, label-free cell imaging, numerical refocusing, and differential interference contrast can be performed [3, 6, 8–11].

Phase is commonly measured using interferometric techniques such as digital holography. For example, in off-axis interferometry, the reference beam is angularly

tilted with respect to the sample beam with wavevector difference Δk [12, 13]. The measured intensity takes the form $I(x,y) = I_r + I_s + 2\sqrt{I_r I_s}\cos(\Delta k \cdot x + \phi(x,y))$, from which phase can be extracted. However, the camera pixel size constrains the highest spatial frequency of the interference pattern and therefore limits the maximum off-axis tilt.

Another interferometric technique, called phase-shifting interferometry, helps to solve this problem. Rather than tilting the reference beam, a phase shift $\delta\phi$ is added to the reference arm [14, 15]. The resulting measured intensity becomes $I(\delta\phi) = I_r + I_s + 2\sqrt{I_r I_s}\cos(\phi + \delta\phi)$. Typically, the reference beam is upshifted in frequency by acousto-optic modulators (AOMs). In [11], a high frame rate camera records images at 5000 fps, which is four times the frequency shift of the reference beam. Each image differs in phase by $\pi/2$. From four consecutive images, phase can be extracted.

Although digital holography is commonly used, it does have its disadvantages. In general, interferometry requires two beams which have to be stabilized. The interference pattern could be very sensitive to table vibrations or temperature fluctuations. The reference arm adds more parts, cost, and complexity. For example, the phase shifting interferometry in [11] requires AOMs to upshift the reference beam and a high frame rate camera to capture the phase-shifted images.

Phase retrieval presents a viable alternative to digital holography for measuring phase. A separate reference beam is not required, which aids stability. The measurements are based on defocused intensity images, which does not require an expensive high frame rate camera. Fewer components are required, which reduces cost.

2.1.2 Enhancing Resolution with Synthetic Aperture Imaging

Regardless of measurement technique, an important concern in any imaging system is resolution, or the ability to resolve fine detail. The objective lens limits the highest spatial frequency that can be captured since it has a finitely sized aperture.

The resolution is roughly λ/NA. In the frequency domain, the spatial frequencies are filtered by a passband which can be described as

$$P(u,v) = \text{circ}\left(\frac{\sqrt{(u/(\lambda f))^2 + (v/(\lambda f))^2}}{NA/\lambda}\right) \tag{2.1}$$

where u and v are spatial coordinates in the back focal plane of the objective lens with units in meters, and f is the focal length of the objective lens. Using this notation, given spatial coordinates (u,v) in the back focal plane of the objective lens, the corresponding spatial frequencies are $\frac{u}{\lambda f}$ and $\frac{v}{\lambda f}$, which are the Fourier transform duals of (x,y).

We can improve resolution if we could capture the spatial frequencies cut off by the lens aperture. To this end consider a plane wave at oblique incidence to a sample,

$$U_{in}^k(x,y) = \exp\left[-j2\pi\left(v_x^k x + v_y^k y\right)\right], \tag{2.2}$$

with wavevector $2\pi\left(v_x^k, v_y^k, v_z^k\right)$. For notational convenience, we let θ_k denote the angle of illumination corresponding to wavevector $2\pi\left(v_x^k, v_y^k, v_z^k\right)$. The field at the back focal plane becomes [3]

$$\begin{aligned} U_f^k(u,v) &= P(u,v)\frac{1}{j\lambda f}\int\int t(x,y)U_{in}^k(x,y)\exp\left[-j\frac{2\pi}{\lambda f}(xu+yv)\right]dxdy \\ &= \frac{1}{j\lambda f}P(u,v)\ T\left(\frac{u}{\lambda f}+v_x^k, \frac{v}{\lambda f}+v_y^k\right) \\ U_f^k\left(u-\lambda f v_x^k, v-\lambda f v_y^k\right) &= \frac{1}{j\lambda f}P\left(u-\lambda f v_x^k, v-\lambda f v_y^k\right)\ T\left(\frac{u}{\lambda f}, \frac{v}{\lambda f}\right) \end{aligned} \tag{2.3}$$

where $T(u,v)$ is the Fourier transform of the sample transmittance $t(x,y)$, and we use Eqs. (2.1) and (2.2). This expression describes the Fourier transform of the field located at the back focal plane (BFP) of the objective. Figure 2.2 depicts the BFP inside the objective, as the plane where light comes to a focus. The obliquely incident plane wave causes the passband to cover a different portion of frequency

space. Summing the fields covered by these shifted passbands yields the synthesized field with an enlargened passband:

$$\begin{aligned} U_f^s(u,v) &= \frac{1}{j\lambda f}\sum_k W^k(u,v)P\left(u-\lambda f v_x^k, v-\lambda f v_y^k\right)\ T\left(\frac{u}{\lambda f},\frac{v}{\lambda f}\right) \\ &= \sum_k W^k(u,v)U_f^k\left(u-\lambda f v_x^k, v-\lambda f v_y^k\right) \end{aligned} \tag{2.4}$$

where we sum over all wavevectors $2\pi\left(v_x^k, v_y^k, v_z^k\right)$, and $W^k(u,v)$ is an angle dependent window function that selects a portion of the spectrum to be added. Section 2.2.2 describes $W^k(u,v)$ in more detail. We note that taking a direct sum by omitting $W^k(u,v)$ is not entirely accurate, since a direct sum would place too much emphasis on the low frequencies and introduce phase aberrations [16]. In effect we are synthetically increasing the numerical aperture of the lens. For this reason researchers refer to this technique as *synthetic aperture imaging*. As a consequence, the imaging system rejects out-of-focus diffraction noise. The resulting image looks cleaner, and techniques like numerical refocusing or differential interference contrast can be digitally implemented [11]. We note that another application, tomographic phase microscopy, also uses the concept of illuminating the sample at oblique angles [17,18], and it is a possible future extension of this work.

2.2 Phase Retrieval Algorithm

2.2.1 General Steps

Phase retrieval is a non-interferometric way of measuring phase. The basic idea is to measure a sequence of defocused intensity images $I_1, ..., I_N$ at N planes and then process these images to extract the phase encoded in the defocus. There are different algorithms that process these defocused images to produce a phase image. Deterministic phase retrieval uses a closed form relation between intensity and phase. Solving a Poisson-type equation yields phase [19–23]. However, this equation relies on the paraxial approximation [19]. In our experiment, we illuminate the sample at

oblique angles with plane waves of the form in Eq. (2.2), which in general will not satisfy the paraxial approximation.

Another class of algorithms is iterative in nature. We can view the intensity measurements as constraints, and we would like to retrieve a complex field satisfying those constraints [24, 25]. We apply an iterative algorithm similar to the single beam multiple intensity reconstruction (SBMIR) technique [26–30]. The general steps are

1. In the first plane, let the complex amplitude $U_1 = \sqrt{I_1}$ with a phase of $\phi_1(x, y) = 0$. Set $n = 1$.

2. Numerically propagate the complex amplitude at the previous plane U_n to the next plane. Extract the phase $\phi_{n+1}(x, y)$.

3. Take the updated complex amplitude as $U_{n+1} = \sqrt{I_{n+1}}\exp\left[j\phi_{n+1}(x, y)\right]$. Increment n by 1.

4. Go to step 2. Iterate until last plane is reached.

We can also add more iterations if desired. For example, the complex amplitude at the last plane can be numerically propagated backwards using a similar update procedure. Convergence is checked by numerically propagating the retrieved field and comparing with measured intensities. In our experiments, we measure a total of 15 planes, as described later in Section 2.3, and we find that numerically propagating forward once and backward once through all the planes is enough for convergence.

The above steps describe how to retrieve phase for one angle of illumination. The idea behind synthetic aperture imaging is to measure phase at multiple angles of illumination. Our proposal is to implement synthetic aperture imaging using phase retrieval. For each angle of illumination, we apply the above procedure to calculate phase. The combination of intensity and phase completely describes the complex field. Then the synthesized field is calculated by summing the complex fields at each angle with the background phases set equal, as described by Eq. (2.4). The *synthesized phase* is the phase of the synthesized field.

By implementing synthetic aperture imaging using phase retrieval, we hope to obtain a more compact experimental setup that has fewer parts, smaller expenses, and more stability. To concisely describe this idea, we refer to it as *synthetic aperture phase retrieval*.

We summarize the synthetic aperture phase retrieval procedure as follows:

1. Select an angle θ_k.
2. Apply the iterative phase retrieval algorithm given above for a single angle. Retrieve the spectrum $U_f^k(u, v)$ (Eq. (2.3)).
3. Go to step 1. Repeat until all angles are measured.
4. Sum the spectra $U_f^k(u, v)$ (Eq. (2.4)) to obtain $U_f^s(u, v)$.
5. Take the inverse Fourier transform of $U_f^s(u, v)$ to obtain the synthesized field.

2.2.2 Stitching of the Synthesized Spectrum

Here we describe the angle dependent window function $W^k(u, v)$ from Eq. (2.4). A simple sum of the retrieved spectra from each angle of illumination would place too much weight on the low frequencies and introduce phase aberrations [16]. To avoid these effects, we filter the retrieved spectra with window functions $W^k(u, v)$. The intuition is that at each angle, the passband shifts to cover a different part of the spectrum, as Eq. (2.3) describes. We would like to capture the general part of the spectrum being measured for each angle. To implement this idea, we partition the synthesized spectrum into angular regions, according to the example presented in [16]. Figure 2.1 shows schematics of how the spectrum can be partitioned. Then the basic idea is to stitch together the synthesized spectrum from the retrieved spectra at each angle of illumination. We illustrate the procedure in the following examples.

Consider the example of measured spectra at 5 total angles. In our experiment we scan the back focal plane of the condenser lens (i.e., the focal plane to the left of the

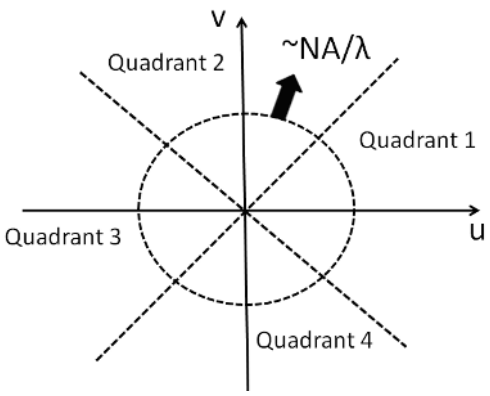

(a) Partition of the synthesized spectrum into quadrants.

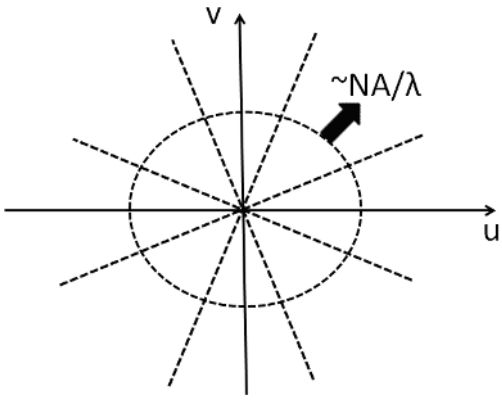

(b) Partition of the synthesized spectrum into octants.

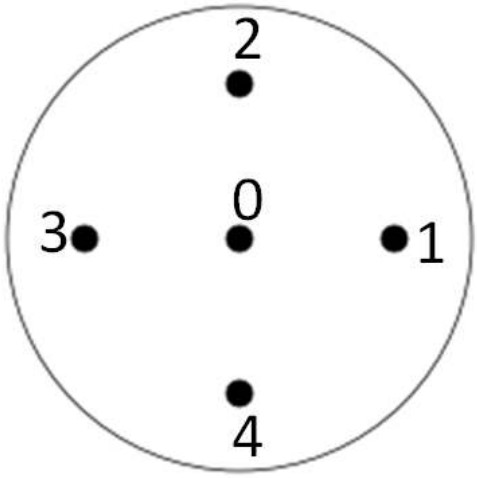

(c) 5 total angles scanned at the back focal plane of the condenser.

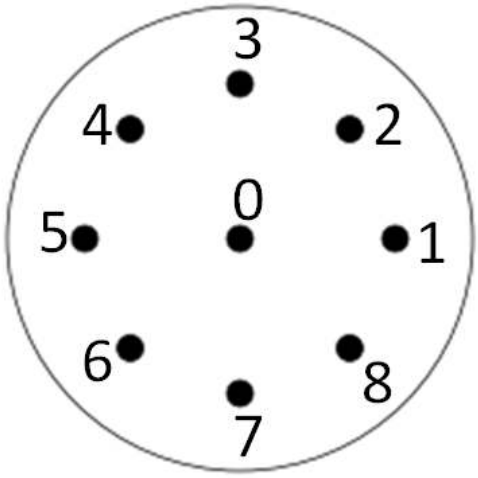

(d) 9 total angles scanned at the back focal plane of the condenser.

Fig. 2.1. Partition of the synthesized spectrum for aperture synthesis.

condenser lens, as depicted in Fig. 2.2) to illuminate the sample at different angles; more details are given in Section 2.3. For convenience, we number the beam positions at the back focal plane in Fig. 2.1(c). When the beam is at position 0, we retrieve the DC or zero degree spectrum $U_f^0(u,v)$, using the notation of Eq. (2.3). At position 1, we retrieve the spectrum $U_f^1(u,v)$ of an obliquely illuminated sample. The main lobe of $U_f^1(u,v)$ lies in quadrant 1 from Fig. 2.1(a). More generally, at position k, we retrieve the spectrum $U_f^k(u,v)$ of the sample illuminated at angle θ_k, and the main lobe of $U_f^k(u,v)$ lies in quadrant k. The synthesized spectrum is composed of selected parts of each spectrum $U_f^k(u,v)$. The central part of the synthesized spectrum (of radius approximately NA/λ) consists of $U_f^0(u,v)$. Outside the central part, quadrant k of the synthesized spectrum consists of $U_f^k(u,v)$. The inverse Fourier transform of the synthesized spectrum yields the synthesized field.

From the above description, we can better understand the factor $W^k(u,v)$ from Eq. (2.4). For $k=0$, $W^0(u,v)$ is a circ function of radius approximately NA/λ, or

$$W^0(u,v) = \begin{cases} 1, & \text{if } \sqrt{u^2+v^2} < \mathrm{NA}/\lambda, \\ 0, & \text{otherwise.} \end{cases} \tag{2.5}$$

For $k>0$, $W^k(u,v)$ is zero everywhere except for a weight of 1 in quadrant k outside a radius of approximately NA/λ, or

$$W^k(u,v) = \begin{cases} 1, & \text{if } (u,v) \in \text{quadrant } k \text{ and } \sqrt{u^2+v^2} > \mathrm{NA}/\lambda, \\ 0, & \text{otherwise.} \end{cases} \tag{2.6}$$

In the case of measured spectra at 9 total angles, we number the beam positions at the back focal plane of the condenser lens in Fig. 2.1(d). The octants in Fig. 2.1(b) are numbered similarly; octant 1 contains the positive u-axis, and octant 3 contains the positive v-axis (numbers are not shown in the figure because of space). When the beam is at position k, we retrieve $U_f^k(u,v)$ for the sample illuminated at angle θ_k, and the main lobe of $U_f^k(u,v)$ lies in octant k. The central part of the synthesized spectrum (of radius approximately NA/λ) consists of $U_f^0(u,v)$. Outside the central

part, octant k of the synthesized spectrum consists of the following weighted sum: $\frac{1}{2}U_f^k(u,v) + \frac{1}{4}U_f^{k-1}(u,v) + \frac{1}{4}U_f^{k+1}(u,v)$, where the indices k, $k-1$, and $k+1$ fall in the range $1,\ldots,8$. Finally the inverse Fourier transform of the synthesized spectrum yields the synthesized field.

We can also describe $W^k(u,v)$ for this case of 9 total angles. For $k=0$, Eq. (2.5) describes $W^0(u,v)$. For $k>0$, $W^k(u,v)$ is zero everywhere except for weights of $1/2$ in octant k and $1/4$ in octants $k-1$ and $k+1$, all outside a radius of approximately NA/λ, or

$$W^k(u,v) = \begin{cases} \frac{1}{2}, & \text{if } (u,v) \in \text{octant } k \text{ and } \sqrt{u^2+v^2} > \text{NA}/\lambda, \\ \frac{1}{4}, & \text{if } (u,v) \in \text{octant } k-1 \text{ and } \sqrt{u^2+v^2} > \text{NA}/\lambda, \\ \frac{1}{4}, & \text{if } (u,v) \in \text{octant } k+1 \text{ and } \sqrt{u^2+v^2} > \text{NA}/\lambda, \\ 0, & \text{otherwise,} \end{cases} \tag{2.7}$$

where the indices k, $k-1$, and $k+1$ fall in the range $1,\ldots,8$, as noted previously. To be fully rigorous, the index $k-1$ should be replaced with $(k-2) \bmod 8 + 1$, so that when $k=1$, the previous index is 8. Similarly, the index $k+1$ should be replaced with $k \bmod 8 + 1$, so that when $k=8$, the next index is 1. However, for simplicity, we use the notation in Eq. (2.7).

2.3 Experimental Setup

Figure 2.2 illustrates the experimental setup for synthetic aperture phase retrieval. A helium-neon (HeNe, $\lambda = 633$ nm) laser serves as the illumination source. Mirror M1 is a motorized gimbal mount, which operates under computer control. It steers the beam at different angles to provide oblique illumination at the sample. After traveling through the condenser lens (Abbe condenser, 1.25 NA) and objective lens (50X, 0.75 NA), the beam is directed through a tube lens and onto a CCD camera, which is mounted on a computer controlled translation stage. We measure a sequence of intensity images by translating the camera along the axial direction. As the stage

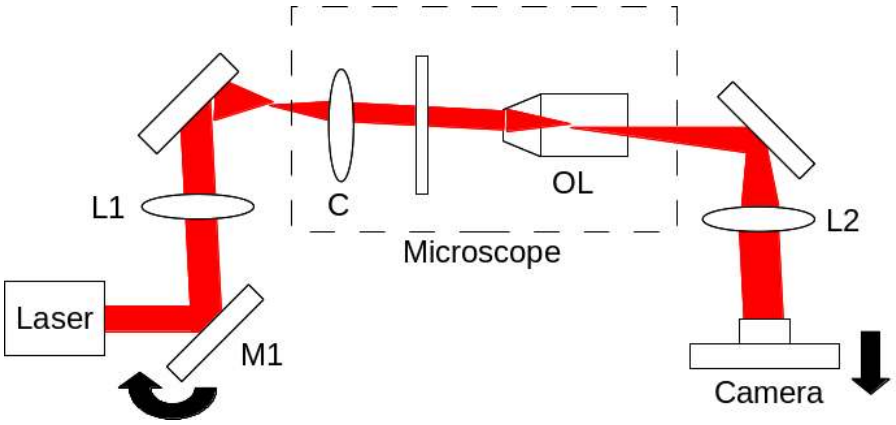

Fig. 2.2. Experimental setup for synthetic aperture phase retrieval. M1: gimbal mount mirror; L1: lens (f = 300 mm); C: condenser lens (NA 1.4); OL: objective lens (NA 0.75); L2: tube lens(f = 200 mm).

moves, the images become defocused. From these defocused images, we apply the iterative phase retrieval algorithm to recover phase.

We note that our experiment uses a 0.75 NA objective; it can be extended to use the 1.4 NA in [11]. We also note that there are very high 1.65 NA objectives, but they require special high index immersion oil that evaporates within a few hours and leaves a crystalline residue. They also require special expensive and fragile coverslips [31]. In this work we aim to demonstrate the principle of using phase retrieval to implement synthetic aperture imaging. Our approach enables resolution enhancement without requiring an expensive high NA objective.

The experimental procedure is to first select an angle of illumination by tilting mirror M1. Then a sequence of defocused intensity images are measured by translating the camera. In our experiments, for each angle we measure 15 intensity images at planes separated by 2.1 μm, where 2.1 μm refers to the sample space, and the planes are symmetric about the focal plane at $z = 0$. We determine the focal plane to be the plane at which the samples look most transparent. More details on how to choose these parameters can be found in [26]. In Fig. 2.3, we show 5 images for one of our samples, 10 μm polystyrene beads ($n = 1.587$) immersed in oil ($n = 1.515$). For a given angle of illumination, it takes about 7 seconds to record 15 intensity images. We note that it should be possible to process these images in real time using a recently developed Kalman filtering algorithm [32–36]. We also note that electronically controllable, variable focus lenses can defocus the image in place of translating the camera, potentially speeding acquisition time [37].

To provide oblique illumination at the sample, the beam scans the back focal plane of the condenser lens, as illustrated in Fig. 2.4. To clarify, Fig. 2.2 depicts the back focal plane (BFP) of the condenser lens to the left of the condenser lens, as the plane where light comes to a focus. Thus Fig. 2.4 portrays focal spots at the BFP. Note at the sample, the beam stays centered and collimated at all angles.

For nonzero degree illumination, the camera translation is no longer parallel to the beam direction. As a result, the images move transversely as the camera moves

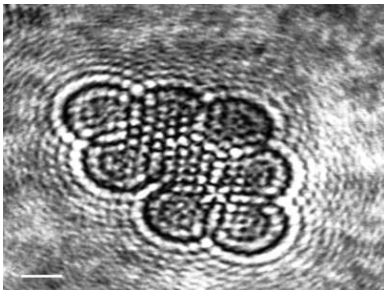

(a) z = -6.3 μm.

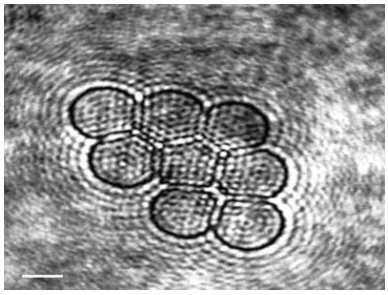

(b) z = -2.1 μm.

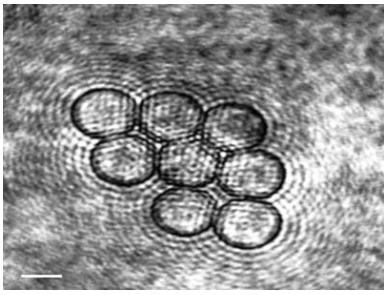

(c) z = 0 μm.

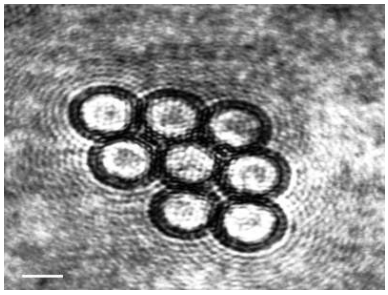

(d) z = 2.1 μm.

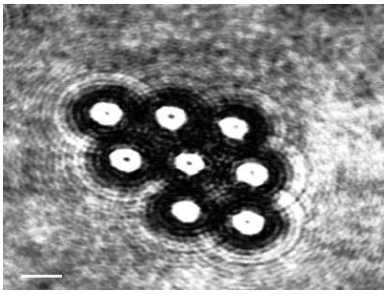

(e) z = 6.3 μm.

Fig. 2.3. Intensity images at zero degrees. Scale bar: 6 μm.

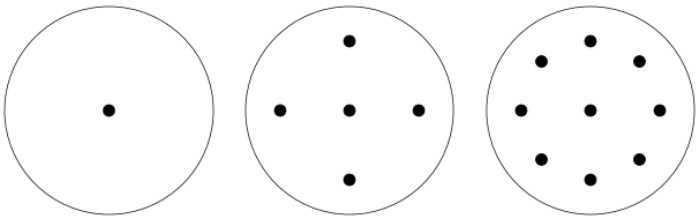

(a) 1 angle. (b) 5 total angles. (c) 9 total angles.

Fig. 2.4. Angular scanning at back focal plane of the condenser lens.

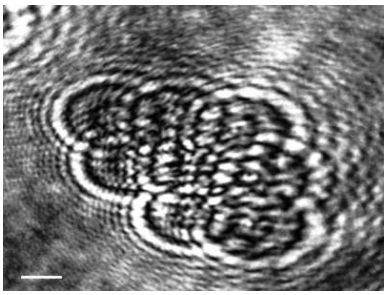

(a) z = -6.3 μm.

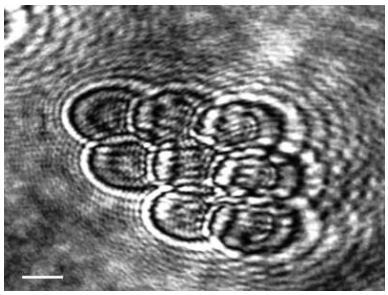

(b) z = -2.1 μm.

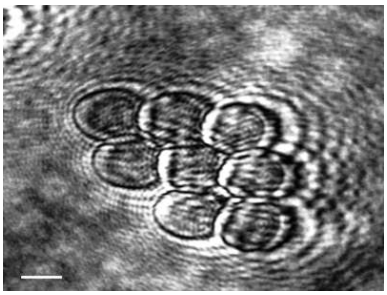

(c) z = 0 μm.

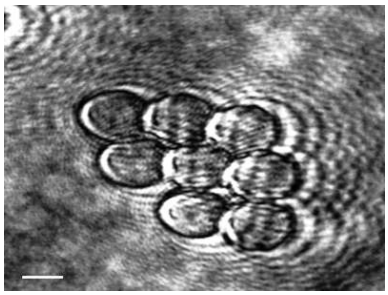

(d) z = 2.1 μm.

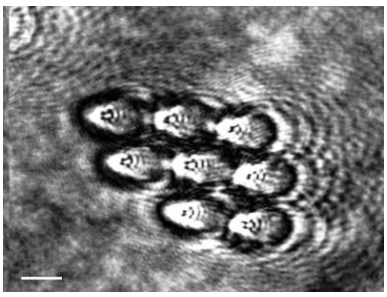

(e) z = 6.3 μm.

Fig. 2.5. Intensity images at 12.3 degrees. Scale bar: 6 μm.

axially. Consequently the images need to be registered. We perform this registration by creating an interference pattern at the camera plane and measuring the beam angle from the fringes. The procedure is described as follows. A beamsplitter taps off a reference beam before the sample. The sample beam is the beam exiting the tube lens. Another beamsplitter combines the reference beam and the sample beam to create an interference pattern at the camera. From the resulting fringes, the angle of the beam can be measured, and we use this angle to register our images. Note that we use the interferometer only for calibration purposes. Once we measure the illumination angle for each control signal sent to tilt mirror M1, the interferometer can be removed from the setup. In Fig. 2.5 we show 5 images taken at 12.3 degrees illumination for one of our samples, 10 μm polystyrene beads, and these images are shown after being registered.

As an example of the angular scanning procedure, Fig. 2.4(b) depicts 4 angles measured around the periphery of the back focal plane, in addition to zero degree illumination (the center dot). In our current configuration, we can illuminate the sample at angles up to 12.3 degrees, measured by the fringe analyis described earlier. We scan the periphery of the back focal plane in an approximate circle so that the largest angle of illumination is 12.3 degrees.

2.4 Phase Measurements

In this section we present two examples of phase measurements to highlight the reduction in diffraction noise and the enhancement of resolution enabled by synthetic aperture imaging. The first experiment uses 10 μm polystyrene beads, both to illustrate our experimental procedure from Section 2.3 and to demonstrate reduction in diffraction noise. These beads have a clearly defined circular shape, and we also show that aperture synthesis enhances this circular profile. In the second experiment, we image small (< 1 μm) dust particles on a glass slide. Due to the smaller feature sizes, we obtain clearer evidence of resolution enhancement.

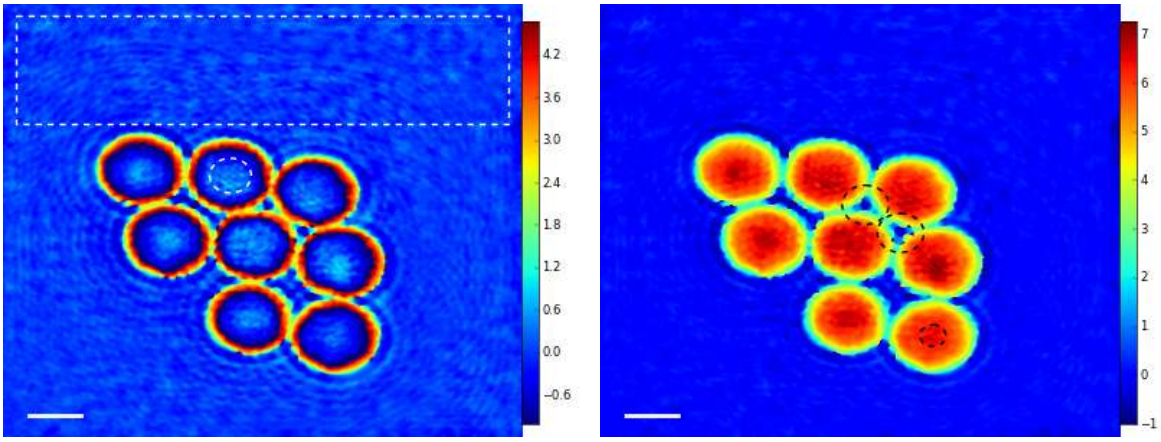

(a) Wrapped phase (rad). The dashed white rectangle and circle will be used for noise analysis.

(b) Unwrapped phase (rad). Two dashed black circles highlight spaces between the beads. The lower dashed circle will be used for calculating average phase.

Fig. 2.6. Test case 1: Phase image at 0 degrees. Scale bar: 6 μm.

2.4.1 Experiment 1: Polystyrene Beads

In our first experiment, we image 10 μm polystyrene beads ($n = 1.587$) immersed in oil ($n = 1.515$). The simplest case occurs when we only measure a phase image at zero degree illumination; in other words, we do not perform synthetic aperture imaging. We perform phase retrieval at zero degrees according to the procedure described in Section 2.3. Figure 2.6 shows the resulting phase image. We can roughly calculate the expected peak phase shift as $\Delta\phi = (2\pi/\lambda)\Delta z(n_{\text{bead}} - n_{\text{bkg}}) = 6.97$ rad, where $\Delta z = 9.75$ μm according to the manufacturer's nominal specifications, $n_{\text{bead}} = 1.587$, and $n_{\text{bkg}} = 1.515$. We estimate the measured peak phase shift by averaging the phase within the black circle in Fig. 2.6(b); the estimated shift is $\Delta\phi = 6.42$ rad, which is reasonably close to the refractive index calculations. The phase retrieval algorithm outputs wrapped phase, and to aid visualization, we also unwrap the results. For phase unwrapping we implement the algorithm presented in [38].

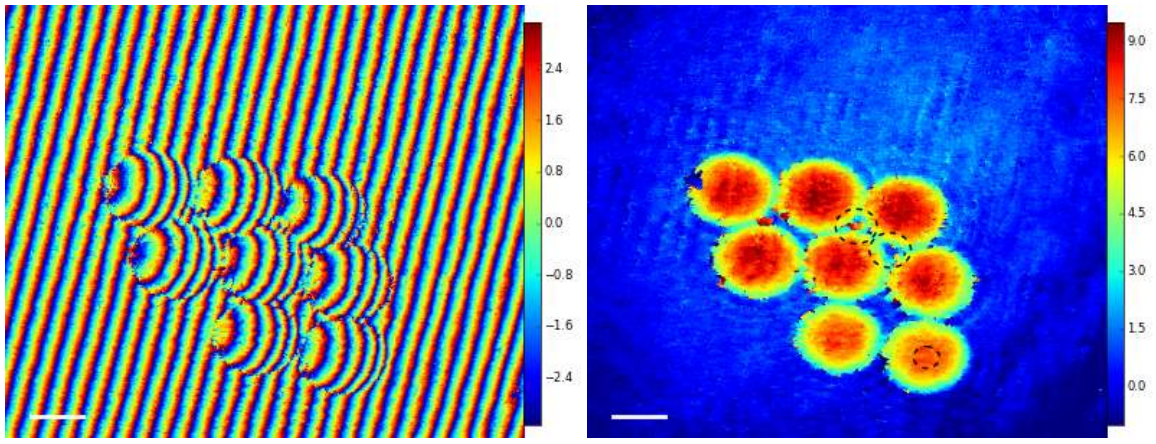

(a) Wrapped phase (rad).

(b) Unwrapped phase (rad). Two dashed black circles highlight spaces between the beads. The lower dashed circle will be used for calculating average phase.

Fig. 2.7. Phase image from off-axis interferometry. Scale bar: 6 μm.

Table 2.1
Phase Retrieval Test Cases

Test Case	Total No. of Angles	Setup Figure	Phase Image Figure
1	1	Fig. 2.4(a)	Fig. 2.6
2	5	Fig. 2.4(b)	Fig. 2.9
3	9	Fig. 2.4(c)	Fig. 2.10

For reference, we also use off-axis interferometry to measure a phase image at zero degree illumination. We tap off a portion of the input beam before the sample as a reference beam, as described in Section 2.3. Figure 2.7 illustrates the off-axis results. We estimate the peak shift by averaging the phase within the black circle in Fig. 2.7(b); the estimated peak shift is $\Delta\phi = 7.57$ rad. However, the image is very noisy, so the phase values are not entirely accurate. More importantly, this figure provides a comparison with the phase retrieval result in Fig. 2.6. In both figures, the circular profiles of the beads look jagged. In addition, the spaces between the beads, highlighed by dashed black circles in Figs. 2.6(b) and 2.7(b), appear partially blended with the beads. We hope to enhance the circular profile of the beads and the resolution between the beads by using synthetic aperture imaging.

We choose this sample of clumps of beads because it exhibits clear diffraction noise. For example, from the defocused intensity images in Fig. 2.3, we can see that the diffraction patterns from each individual bead interferes with those of other beads. Diffraction noise appears in Fig. 2.6 as diffraction rings and speckle-like patterns inside the beads, which is most clearly seen in the wrapped phase image. Similarly, we can discern some speckle-like patterns inside the beads in Fig. 2.7. We hope to reduce this diffraction noise with synthetic aperture imaging.

Next we perform synthetic aperture imaging by illuminating the sample at multiple angles. We examine the synthesized phase images for the different numbers of angles listed in Table 2.1. Figure 2.8 shows a phase image captured at 11.0 degrees illumination. To aid visualization, we also unwrap the phase. Although there are

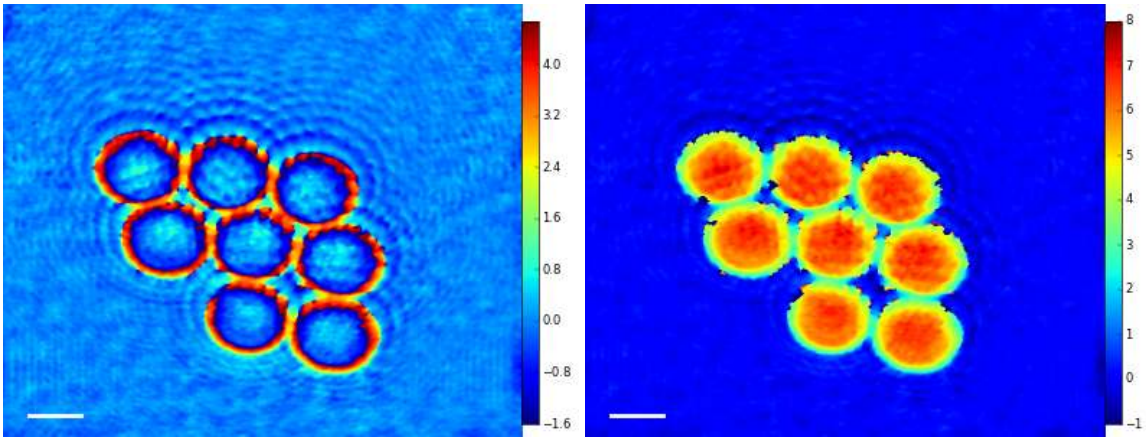

(a) Wrapped phase (rad). (b) Unwrapped phase (rad).

Fig. 2.8. Phase image at 11.0 degrees. Scale bar: 6 μm.

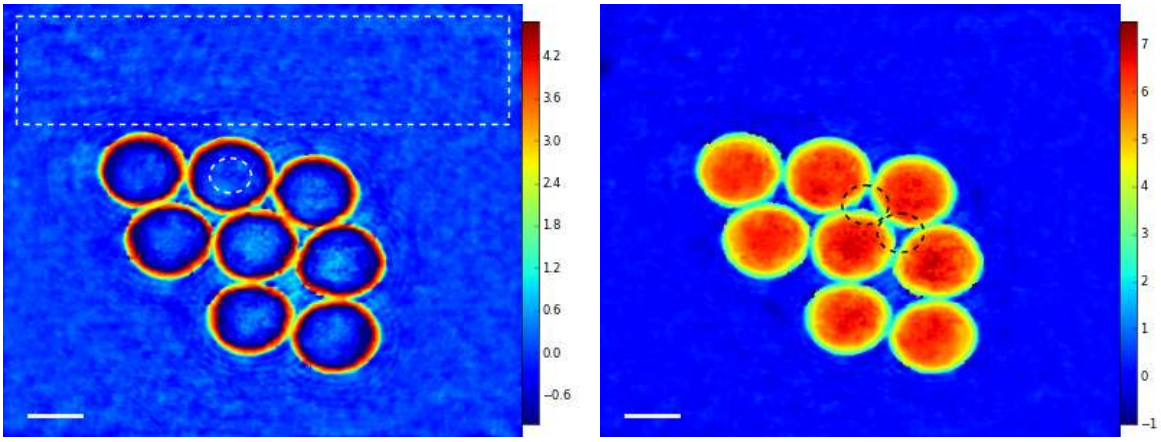

(a) Wrapped phase (rad). The dashed white rectangle and circle will be used for noise analysis.

(b) Unwrapped phase (rad). Two dashed black circles highlight spaces between the beads.

Fig. 2.9. Test case 2: Synthesized phase image with 5 total angles. Scale bar: 6 μm.

some unwrapping errors, the figure illustrates the basic idea. We note that synthetic aperture imaging does not require phase unwrapping; the spectra are stitched together as described in Section 2.2.2. Since the beam is oblique to the camera, the beads appear slightly elongated [11, 17]. As in the case of zero degree illumination, speckle-like patterns inside the beads and diffraction rings appear. To the best of our knowledge, this work is the first experimental demonstration of phase retrieval on an obliquely illuminated sample.

For test case 2, we measure a total of 5 angles, as noted in Table 2.1. We perform synthetic aperture imaging by adding the angular spectra according to Eq. (2.4), together with the window functions from Eqs. (2.5) and (2.6). The resulting synthesized phase is illustrated in Fig. 2.9. We see that diffraction noise features, such as the diffraction rings and the speckle-like patterns inside the beads, have been reduced compared to test case 1, which can be seen most clearly from the wrapped phase images.

For test case 3, we measure a total of 9 angles as noted in Table 2.1. The angular spectra are added according to Eq. (2.4), together with the window functions from

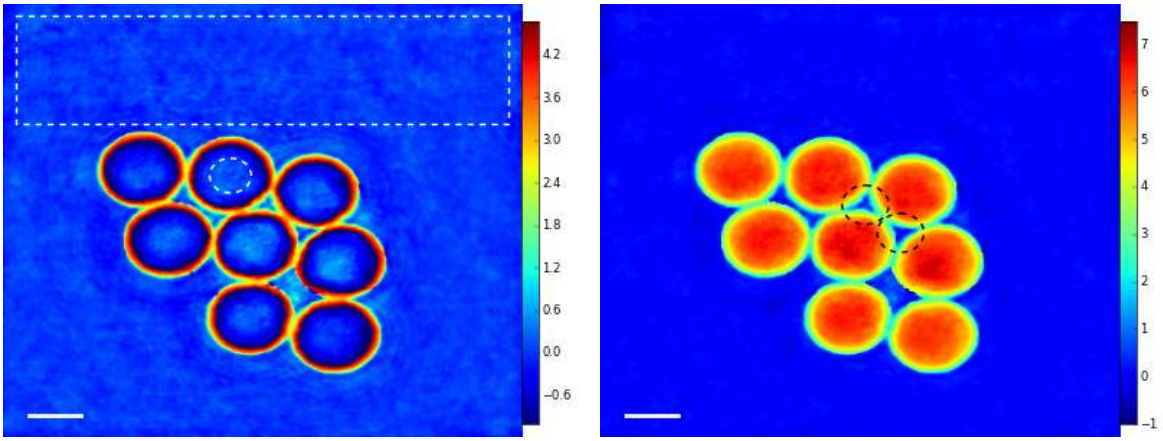

(a) Wrapped phase (rad). The dashed white rectangle and circle will be used for noise analysis.

(b) Unwrapped phase (rad). Two dashed black circles highlight spaces between the beads.

Fig. 2.10. Test case 3: Synthesized phase image with 9 total angles. Scale bar: 6 μm.

Table 2.2
Phase Speckle and Background Noise Comparisons

Test Case	Phase Speckle Noise σ_s^2 $\left(\text{rad}^2\right)$	% Reduction in σ_s^2 Compared to Case 1	Background Noise σ_b^2 $\left(\text{rad}^2\right)$	% Reduction in σ_b^2 Compared to Case 1
1	$\sigma_s^2 = 8.30 \times 10^{-2}$	0%	$\sigma_b^2 = 1.75 \times 10^{-2}$	0%
2	$\sigma_s^2 = 3.36 \times 10^{-2}$	59%	$\sigma_b^2 = 1.51 \times 10^{-2}$	14%
3	$\sigma_s^2 = 1.49 \times 10^{-2}$	82%	$\sigma_b^2 = 7.68 \times 10^{-3}$	56%

Eqs. (2.5) and (2.7). Figure 2.10 shows the synthesized phase. The diffraction noise features (diffraction rings and speckle-like patterns inside the beads) appear more reduced than test case 2. As more angles are measured, the passband in Eq. (2.1) shifts to cover different portions of frequency space, which yields the different angular fields in Eq. (2.3). As a result, when these angular fields are summed in Eq. (2.4), the synthesized field contains an enlargened passband. Hence, we would expect this improvement in diffraction noise with more angles. In addition, the circular shape of the beads becomes progressively less jagged as more angles are measured, as Figs. 2.6(a), 2.9(a), and 2.10(a) show. We also notice the spaces between the beads become increasingly distinguishable as more angles are added; these spaces are highlighted by dashed black circles in Figs. 2.6(b), 2.9(b), and 2.10(b).

Next we examine a quantitative comparison of the DC case (test case 1) and the synthetic aperture cases (test cases 2 and 3). We measure the phase speckle noise σ_s^2 inside the bead (dashed circle) for Fig. 2.6(a) $\left(\sigma_s^2 = 8.30 \times 10^{-2} \text{ rad}^2\right)$ and for Figs. 2.9(a) and 2.10(a) $\left(\sigma_s^2 = 3.36 \times 10^{-2} \text{ and } 1.49 \times 10^{-2} \text{ rad}^2 \text{ respectively}\right)$; the phase speckle noise reduces by 59% and 82% respectively, compared to the DC case. We also measure the background noise σ_b^2 inside the dashed rectangle for Fig. 2.6(a) $\left(\sigma_b^2 = 1.75 \times 10^{-2} \text{ rad}^2\right)$ and for Figs. 2.9(a) and 2.10(a) ($\sigma_b^2 = 1.51 \times 10^{-2}$ and 7.68×10^{-3} rad^2 respectively); the background noise reduces by 14% and 56%

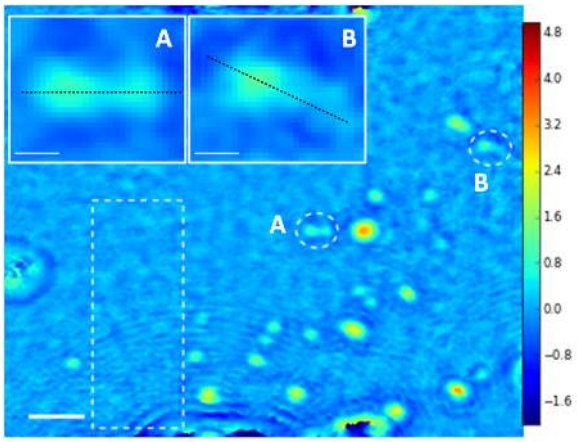

(a) DC phase (rad). Scale bar: 6 μm. Inset scale bar: 1 μm.

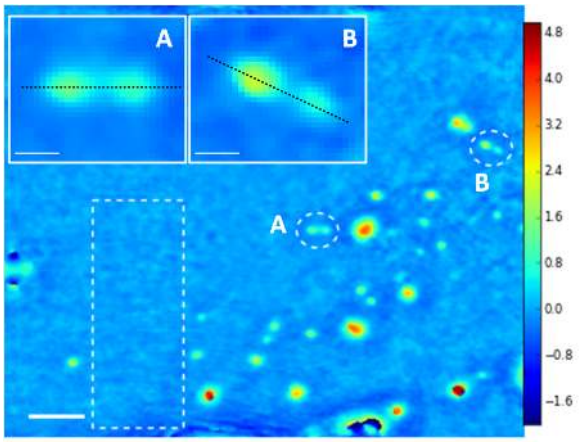

(b) Synthesized phase (rad). Scale bar: 6 μm. Inset scale bar: 1 μm.

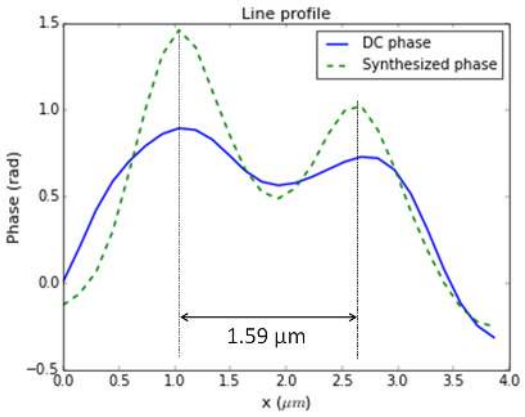

(c) Line profile from inset A.

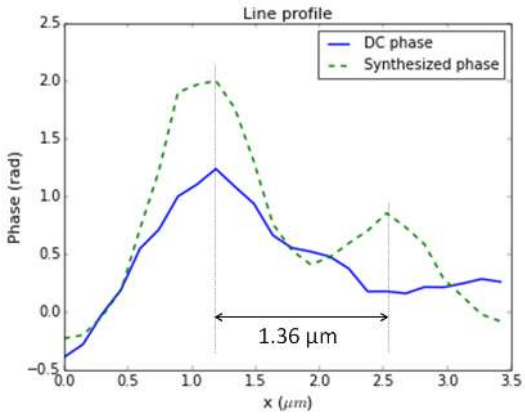

(d) Line profile from inset B.

Fig. 2.11. Resolution enhancement of particles on a glass slide.

respectively, compared to the DC case. Table 2.2 summarizes these results. We see that adding more angles reduces the diffraction noise.

2.4.2 Experiment 2: Particles on a Glass Slide

In the second experiment, we image small (< 1 μm) dust particles on a glass slide. Similar to the demonstration of resolution enhancement in [16], we examine particles

that are close to the resolution limit of the imaging system, with the goal of showing better differentiation between particles with aperture synthesis. A total of 9 angles are measured, and the retrieved spectra from each angle are added according to Eq. (2.4), together with the window functions from Eqs. (2.5) and (2.7).

To demonstrate resolution enhancement, we compare the DC or zero degree phase in Fig. 2.11(a) with the synthesized phase in Fig. 2.11(b). In general, the synthesized phase looks sharper. We highlight two pairs of particles that are hard to distinguish with dashed white circles. To facilitate comparison, we plot line profiles along the lines shown in insets A and B. As the profiles in Figs. 2.11(c) and 2.11(d) indicate, the synthesized phase shows increased contrast between the two particles, allowing them to be better differentiated.

We can estimate the resolution of the setup from the line profiles in Fig. 2.11. In general, the spatial resolution is determined by the NA and wavelength as

$$\delta = \frac{\kappa\lambda}{NA} \tag{2.8}$$

where the factor κ depends on experimental parameters such as the signal to noise ratio of the detector [16]. For our experiment, $\lambda = 633$ nm and NA $= 0.75$. We estimate the resolution as $\delta = 1.59$ μm from Fig. 2.11(c), where two particles look close to the resolution limit for the DC phase. Using aperture synthesis, we expect this resolution to improve to

$$\delta = \frac{\kappa\lambda}{NA + \sin\,\theta_{\text{illum}}} \tag{2.9}$$

where θ_{illum} is the angle of illumination used for the synthetic aperture. We take $\theta_{\text{illum}} = 12.3$ degrees, which is the largest angle of illumination for our experiment. From Eq. (2.9), we expect the resolution to improve to $\delta = 1.24$ μm. Indeed, Fig. 2.11(d) shows two particles separated by 1.36 μm which become distinguishable after aperture synthesis.

We also measure the reduction in diffraction noise, as we did for the polystyrene beads in Table 2.2. Inside the dashed white rectangles in Figs. 2.11(a) and 2.11(b),

we calculate the background noise for the DC phase $\left(\sigma_b^2 = 2.05 \times 10^{-2} \text{ rad}^2\right)$ and the synthesized phase $\left(\sigma_b^2 = 9.12 \times 10^{-3} \text{ rad}^2\right)$; the background noise reduces by 55%. As a consequence, the diffraction rings near the bottom of Fig. 2.11(a) disappear, enabling other particles to be better distinguished.

2.5 Conclusion

We have demonstrated the principle of using phase retrieval to implement synthetic aperture imaging. Synthetic aperture imaging reduces diffraction noise and enhances resolution by effectively increasing the numerical aperture. Previously this technique has relied on digital holography for phase measurements. By obviating the need for a reference arm, this approach provides a more compact, less expensive, and more stable setup. Our demonstration paves the way for other applications such as tomographic phase microscopy to be enabled by phase retrieval.

3. SYNTHETIC APERTURE MICROSCOPY BASED ON REFERENCELESS PHASE RETRIEVAL WITH AN ELECTRICALLY TUNABLE LENS

Phase imaging microscopy, based either on holography or non-holographic methods such as phase retrieval, has seen considerable recent attention. Phase retrieval offers the advantage of being free of a reference arm and enables a more stable and compact setup. We present an optical setup which provides enhanced resolution by implementing synthetic aperture imaging based on phase retrieval using an electrically tunable lens (ETL). The ETL is a more compact and less expensive alternative to computerized translation stages and spatial light modulators. Before applying phase retrieval, we discuss a general calibration algorithm which performs image registration, corrects for magnifications, and determines the axial locations of image planes. Finally we obtain resolution-enhanced images of a phase grating and of cells to demonstrate the practical application of our technique.

3.1 Introduction

Imaging phase objects, such as transparent biological specimens, is an important application in microscopy. A common way to view transparent samples is to use fluorescence; well-known methods include confocal, 4π, structured illumination, and stimulated emission depletion microscopy [1,39,40]. A drawback is that some samples may not be fluorescent or are not easily fluorescently tagged. Phase objects have an important property that they induce phase shifts as light diffracts through them. By converting these phase shifts to intensity variations, techniques like phase contrast or differential interference contrast (DIC) can qualitatively image phase, which acts as a label-free contrast agent [41–43]. More recent efforts to quantify phase offer the

advantage of measuring cell thickness [9], quantifying path lengths [13, 44], numerically focusing samples [12, 14, 45], and viewing 3D cellular structure [17]. Holography is a commonly used technique to measure phase, but it requires a reference arm which makes it sensitive to vibrations and temperature changes. Referenceless single beam techniques compute phase from a sequence of diffraction patterns. Some examples of diffraction patterns include defocused images [21, 25, 26], spatially modulated illumination [2, 46], angular illumination [47], and structured illumination [16, 48]. Defocusing images is attractive because it can be simply implemented by moving a camera on a translation stage [27], applying a lens function on a 2D spatial light modulator (SLM) [49, 50], or changing the focal length of an electrically tunable lens (ETL) [51–54]. Of these different ways to defocus, the ETL is a compact, relatively inexpensive option that is free of mechanical motion, in contrast to computerized translation stages or 2D SLMs.

The resolution of phase objects can be improved using different techniques. Some holographic techniques include off-axis illumination [11, 55], structured illumination [16, 56], or shorter wavelength sources [57]. Synthetic aperture imaging uses off-axis illumination to capture higher spatial frequencies that would be cut-off by the finite aperture of the objective lens. For example, electric field images can be captured at different angles based on phase-shifting interferometry [11]. Alternatively, non-holographic techniques can be based on referenceless phase retrieval, which has the advantage of being a more stable and compact setup without requiring expensive components such as a high frame rate camera. Some examples of non-holographic methods are based on synthetic aperture imaging [58,59], structured illumination [60], and angular illumination [47].

In this work, we propose a variant on synthetic aperture microscopy based on referenceless phase retrieval. The proposed technique uses an electrically tunable lens (ETL) to defocus images, which eliminates the mechanical motion of the translation stage and avoids the cost and bulkiness of a spatial light modulator. As part of this technique, we develop a calibration algorithm to register images, correct for image

magnifications, and compute the axial locations of image planes. This algorithm more generally applies to other experiments which require precise alignment of images or image magnification to be controlled. For example, transport-of-intensity phase microscopy with an ETL [54] and 3D light-sheet microscopy with a tunable lens [52] are sensitive to image alignment and magnification and could benefit from this algorithm.

3.2 Experiment Description

3.2.1 Setup

Figure 3.1(a) illustrates the experimental setup. Mirror M1 tilts to scan the sample at different angles. After traveling through the objective lens, light passes through the ETL (Optotune, EL-10-30-C-VIS-LD-MV) with variable focal length controlled by a user-supplied input current. The focal length can be tuned from -600 mm to infinity to 170 mm over a current range from 0 mA to 300 mA [61]. In this non-telecentric configuration, image magnification varies with ETL focal length f_{ETL}. In theory, for thin lenses, the magnification factor γ, which results in a scaled image $I(\gamma x, \gamma y)$, depends on f_{ETL} as

$$\gamma = \frac{f_{\mathrm{ETL}} f_{\mathrm{TL}}}{f_{\mathrm{OL}}(f_{\mathrm{ETL}} + f_{\mathrm{TL}} - d_{\mathrm{ETL/TL}})} \tag{3.1}$$

where f_{TL} and f_{OL} are focal lengths of the tube and objective lenses, and $d_{\mathrm{ETL/TL}}$ is the distance between the ETL and TL [62]. Similarly, we can make a theoretical calculation of the axial location z of an image plane for a given f_{ETL}. Note z refers to the distance between the sample plane and the plane which would be imaged onto the CCD for a given f_{ETL}. In Fig. 3.1(c), the sample is located at $z = 0$. An image taken at $z = 0$ refers to the sample imaged onto the CCD; the sample is in focus. In theory, z depends on f_{ETL} as [62]

$$z = \frac{f_{\mathrm{TL}}(d_{\mathrm{ETL/TL}} - f_{\mathrm{ETL}})}{\gamma(d_{\mathrm{ETL/TL}} - (f_{\mathrm{ETL}} + f_{\mathrm{TL}}))} = \frac{f_{\mathrm{OL}}(f_{\mathrm{ETL}} - d_{\mathrm{ETL/TL}})}{f_{\mathrm{ETL}}}. \tag{3.2}$$

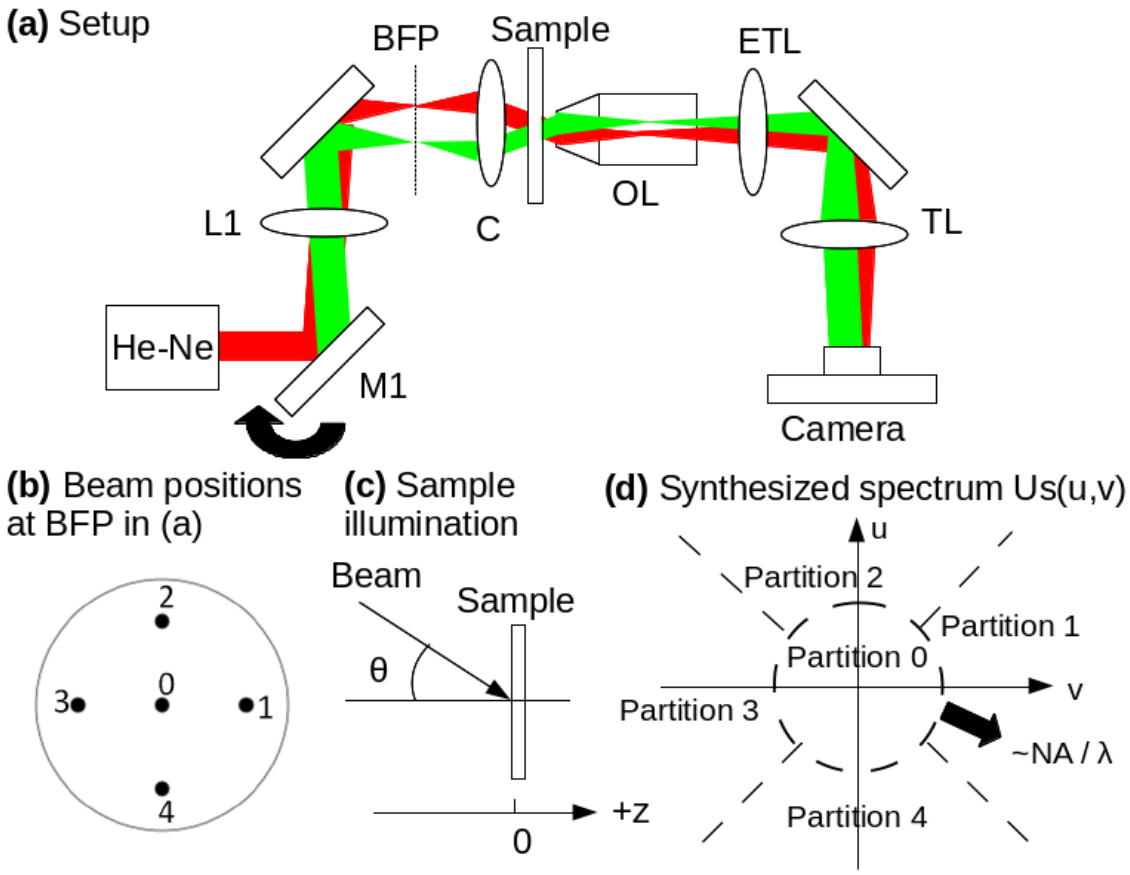

Fig. 3.1. (a) Setup. The red and green rays trace 2 angles of illumination. He-Ne: 633 nm; M1: gimbal mount mirror; L1: lens (f = 300 mm); BFP: back focal plane of the condenser lens; C: condenser lens; OL: objective lens (50X, NA 0.75); ETL: electrically tunable lens; TL: tube lens (f = 200 mm). (c) θ is the angle of illumination. (d) We divide $U_s(u, v)$ into partitions. In partition k, we set $U_s(u, v) = U_k(u, v)$, where k is the beam position at the BFP in (b), and $U_k(u, v)$ is the corresponding spectrum.

However, the calculations in Eqs. (3.1) and (3.2) require precise knowledge of physical parameters such as $d_{\mathrm{ETL/TL}}$ and f_{ETL}. Rather than trying to make precise measurements, we describe a practical algorithm to determine γ and z.

3.2.2 Overview of the Calibration Algorithm

Next we describe a calibration algorithm which will correct for image magnifications arising from non-telecentricity, as well as register images and determine the axial locations of image planes. The algorithm sequentially optimizes over these unknown parameters. We note that this sequential strategy is inspired by the algorithm in [50]. As an input to the calibration routine, we measure the complex electric field at the focal plane of the OL ($z = 0$ in Fig. 3.1(c)) over all angles to be scanned. We can make this measurement using off-axis interferometry with Fourier filtering [13, 44]. After calibration, extra components required for the interferometer can be removed.

In this work we measure five total angles: one at DC ($\theta = 0^\circ$ in Fig. 3.1(c)) plus four angles around the periphery of the back focal plane of the condenser lens (Fig. 3.1(b)), spaced by 90° and scanned in an approximate circle so that the largest illumination angle is $\theta = 12.7^\circ$. Of course this technique can include more angles. Let us denote the fields measured in the calibration step as $u_0^c(x, y), \ldots, u_4^c(x, y)$. For example, $u_0^c(x, y)$ is the field at DC illumination, while $u_1^c(x, y)$ corresponds to the field measured when the beam is at position 1 (Fig. 3.1(b)) at the BFP (Fig. 3.1(a)).

For a given angle of illumination or beam position k at the BFP, the algorithm begins by numerically propagating the complex electric field $u_k^c(x, y)$ to different z planes, where the user supplies an initial guess of the axial locations in sample space. Let $\hat{z}_1, \ldots, \hat{z}_{N_{\mathrm{im}}}$ denote the current guess of the axial locations, where N_{im} is the total number of images for a given angle; z refers to the distance between the sample plane and the plane which would be imaged onto the CCD for a given ETL setting. Let us represent the true axial locations as $z_1, \ldots, z_{N_{\mathrm{im}}}$. In our experiment we measure 11 images for each angle ($N_{\mathrm{im}} = 11$), with each image corresponding to a different focal

length of the ETL. Note that changing the ETL focal length equivalently defocuses the sample to a different z (Fig. 3.1(c)). After numerical propagation, we obtain a set of simulated images $\{I_s(x, y; \hat{z}_i) : i = 1, \ldots, N_{\text{im}}\}$. Our goal is to match the set of simulated images $\{I_s(x, y; \hat{z}_i) : i = 1, \ldots, N_{\text{im}}\}$ with the set of measured images $\{I_m(x, y; z_i) : i = 1, \ldots, N_{\text{im}}\}$. During calibration we will refine our guess of $\hat{z}_i$.

3.2.3 Strategy for Algorithm Convergence

When trying to match 2 images, the algorithm may get stuck in a local minimum. The best way to avoid a local minimum is to start with an initial guess that matches the 2 images as closely as possible. Then the job of the algorithm is to refine the initial guess to optimize the cross-correlation ρ

$$\rho = \frac{1}{N} \sum_{x,y} \frac{(I_m(x, y; z_i) - \bar{I}_m)(I_s(x, y; \hat{z}_i) - \bar{I}_s)}{\sigma_m \sigma_s} \tag{3.3}$$

where $\bar{I}_m$ and $\bar{I}_s$ denote average intensities, σ_m and σ_s are intensity standard deviations for the measured and simulated images, respectively, and N is the total number of pixels. Cross-correlation works best on objects with information-rich features such as clear patterns. We find that we can make a good initial guess by assuming that the image shifts, magnifications, and defocus are linearly proportional to the applied current on the ETL, i_{ETL}.

The physical intuition is that as the ETL focal length changes, the lens deforms to different shapes, causing the beam to deflect. For example, suppose a deflection of δx results in a shifted image $I(x + \delta x, y)$. As a rough geometrical approximation, we can estimate the shift amount δx to be proportional to i_{ETL}, f_{TL}, and the angle of illumination θ:

$$\delta x \propto i_{\text{ETL}} f_{\text{TL}} \tan\theta \tag{3.4}$$

where θ can be measured in a calibration step using off-axis interferometery.

Similarly, given a magnified image $I(\gamma x, \gamma y)$, we can roughly predict image magnification γ as a linear function of i_{ETL}. In theory, Eq. (3.1) describes γ as a function

of physical parameters. For an initial guess, we start with the simplest relation that γ is linearly proportional to i_{ETL}:

$$\gamma \propto i_{\mathrm{ETL}}. \tag{3.5}$$

To make an initial guess for the axial location of an image plane, suppose an image is located at z, which we represent as $I(x, y; z)$. In theory, Eq. (3.2) computes z in terms of physical parameters. Since measuring these parameters is difficult, instead we start with the simplest possible model that z is proportional to i_{ETL}:

$$z \propto i_{\mathrm{ETL}}. \tag{3.6}$$

One way to make the guesses in Eqs. (3.4)-(3.6) more precise is to initially determine δx, γ, and z by rough inspection as i_{ETL} varies. Experimentally, we find that this strategy brings these parameters close enough to the actual values so that the calibration algorithm, described below, can compute the correct values.

3.2.4 Registering Images

According to the pixel size δ_p of the sensor array, the intensities $I(x, y)$ are sampled as $I[m, n] = I(m\delta_p, n\delta_p)$. The sampled simulated and measured images can be represented as

$$I_s[m, n; \hat{z}_i] = I_s(m\delta_p, n\delta_p; \hat{z}_i) \tag{3.7}$$

and

$$I_m[m, n; z_i] = I_m(m\delta_p, n\delta_p; z_i). \tag{3.8}$$

The next step in the calibration algorithm is to shift the measured images in the horizontal and vertical directions to optimally match the simulated intensity images by maximizing ρ_1:

$$\rho_1(\Delta_m, \Delta_n) = \frac{1}{N} \sum_{m,n} \frac{(I_m[m + \Delta_m, n + \Delta_n; z_i] - \bar{I}_m)(I_s[m, n; \hat{z}_i] - \bar{I}_s)}{\sigma_m \sigma_s} \tag{3.9}$$

where Δ_m and Δ_n are the pixel shift amounts to be tested. We find that trying values $-11 \leq \Delta_m, \Delta_n \leq 11$ gives good, convergent results. Once we find the optimal shifts Δ_m^* and Δ_n^* as

$$(\Delta_m^*, \Delta_n^*) = \underset{\Delta_m, \Delta_n}{\operatorname{argmax}} \rho_1 (\Delta_m, \Delta_n), \tag{3.10}$$

we update the measured image as

$$I_m[m, n; z_i] \leftarrow I_m[m + \Delta_m^*, n + \Delta_n^*; z_i]. \tag{3.11}$$

3.2.5 Rescaling Images

Next we would like to find the magnification γ that maximizes the cross-correlation ρ_2:

$$\rho_2(\gamma) = \frac{1}{N} \sum_{m,n} \frac{(I_m[\gamma m, \gamma n; z_i] - \bar{I}_m)(I_s[m, n; \hat{z}_i] - \bar{I}_s)}{\sigma_m \sigma_s} \tag{3.12}$$

The general strategy is to try different values for γ and find the optimal γ^* that maximizes ρ_2. Since γm or γn may not be integer-valued, the magnified image $I_m[\gamma m, \gamma n; z_i]$ can be computed using bicubic interpolation. We find that trying values in the range $0.99 \leq \gamma \leq 1.01$, sampled in increments of 0.002, yields convergent results. We compute the optimal γ^* as

$$\gamma^* = \underset{\gamma}{\operatorname{argmax}} \rho_2 (\gamma) \tag{3.13}$$

and update the measured image with the optimal γ^*:

$$I_m[m, n; z_i] \leftarrow I_m[\gamma^* m, \gamma^* n; z_i]. \tag{3.14}$$

3.2.6 Calculating Axial Locations of Image Planes

Next we would like to find the amount of defocus Δ_z that maximizes the cross-correlation ρ_3

$$\rho_3 (\Delta_z) = \frac{1}{N} \sum_{m,n} \frac{(I_m[m, n; z_i] - \bar{I}_m)(I_s[m, n; \hat{z}_i + \Delta_z] - \bar{I}_s)}{\sigma_m \sigma_s}. \tag{3.15}$$

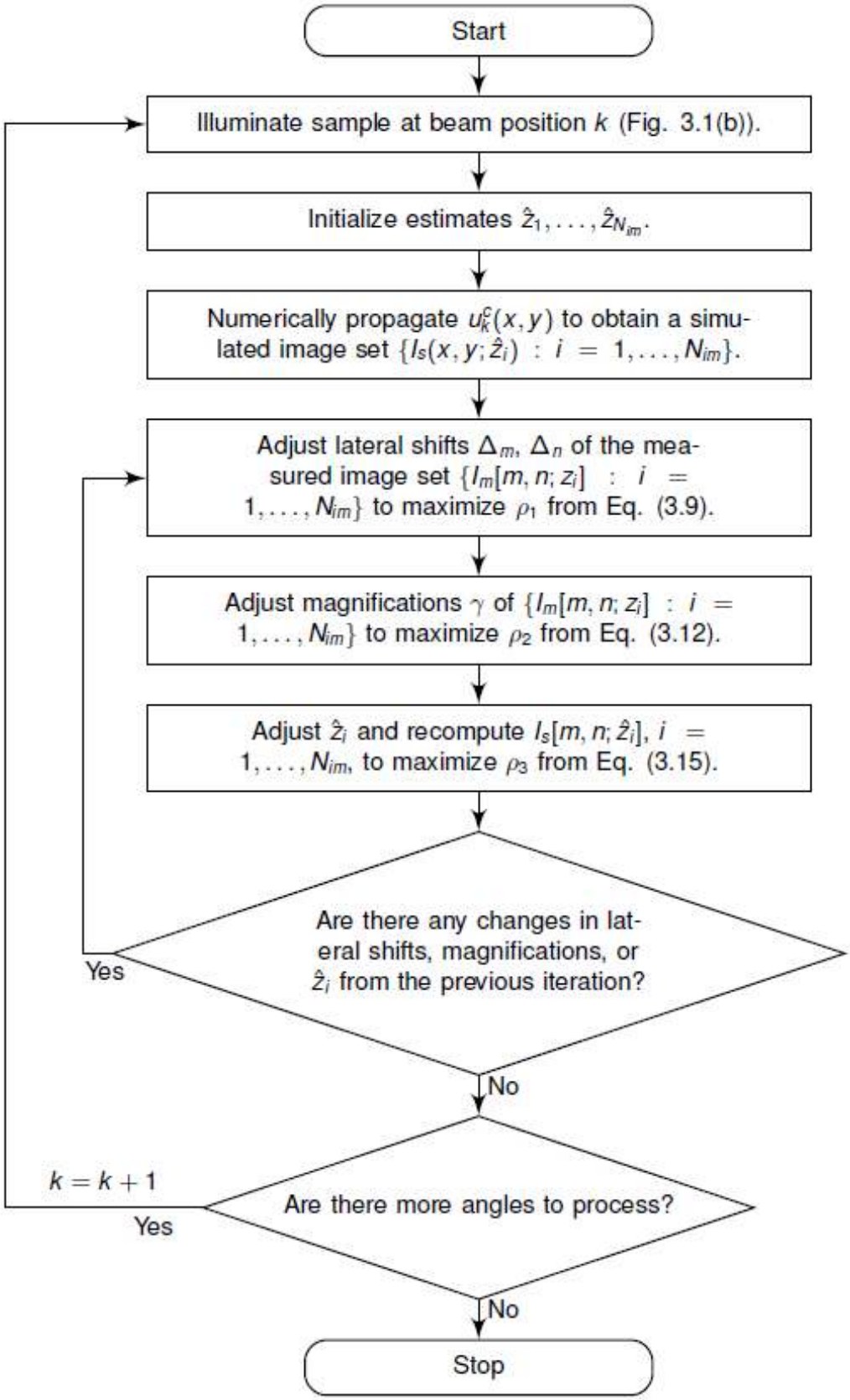

Fig. 3.2. Flowchart of the calibration algorithm. The program performs image registration, corrects for magnifications, and determines the axial locations of image planes.

Using a similar strategy as before, we test different values of Δ_z in the range $-1\ \mu\text{m} \leq \Delta_z \leq 1\ \mu\text{m}$, sampled in increments of 0.1 μm. We find that trying these values yields a convergent algorithm. For each value of Δ_z, we simulate propagation of the complex electric field $u_k^c(x, y)$ to $\hat{z}_i + \Delta_z$, measured in the calibration step as described in Section 3.2.2. We compute the optimal Δ_z^* as

$$\Delta_z^* = \underset{\Delta_z}{\text{argmax}}\, \rho_3 \left(\Delta_z\right). \tag{3.16}$$

Then we update the axial location $\hat{z}_i$ of image plane i with the optimal value Δ_z^*:

$$\hat{z}_i \leftarrow \hat{z}_i + \Delta_z^*, \tag{3.17}$$

and the simulated image is updated with the optimal value Δ_z^*:

$$I_s[m, n; \hat{z}_i] \leftarrow I_s[m, n; \hat{z}_i + \Delta_z^*]. \tag{3.18}$$

After this update, the algorithm loops to repeat the steps of registering and rescaling images and optimizing image axial locations until there is no change in the parameters. In other words, for each image, the calibration loop terminates when $\Delta_m^*, \Delta_n^* = 0$, $\gamma^* = 1$, and $\Delta_z^* = 0$. Figure 3.2 summarizes this procedure in a top-level flowchart.

3.2.7 Calibration Example

To illustrate the action of the calibration program, we examine a phase grating sample. The sample consists of gratings with different periods patterned in PMMA film ($n = 1.49$) on a glass substrate. For calibration, we examine a portion of the sample with a 12 μm grating and display measured images before and after calibration, as well as simulated (numerically propagated) images after calibration, in Figs. 3.3(a)-(c). We see that the shifts and magnifications have been corrected so that the measured and simulated images agree in Figs. 3.3(b) and (c).

To retrieve phase, we need to know how much each image is defocused along the z axis. Figures 3.3(d) and (e) plot the axial locations and magnifications for DC illumination, values typical over all angles. We designate the middle plane (plane 6)

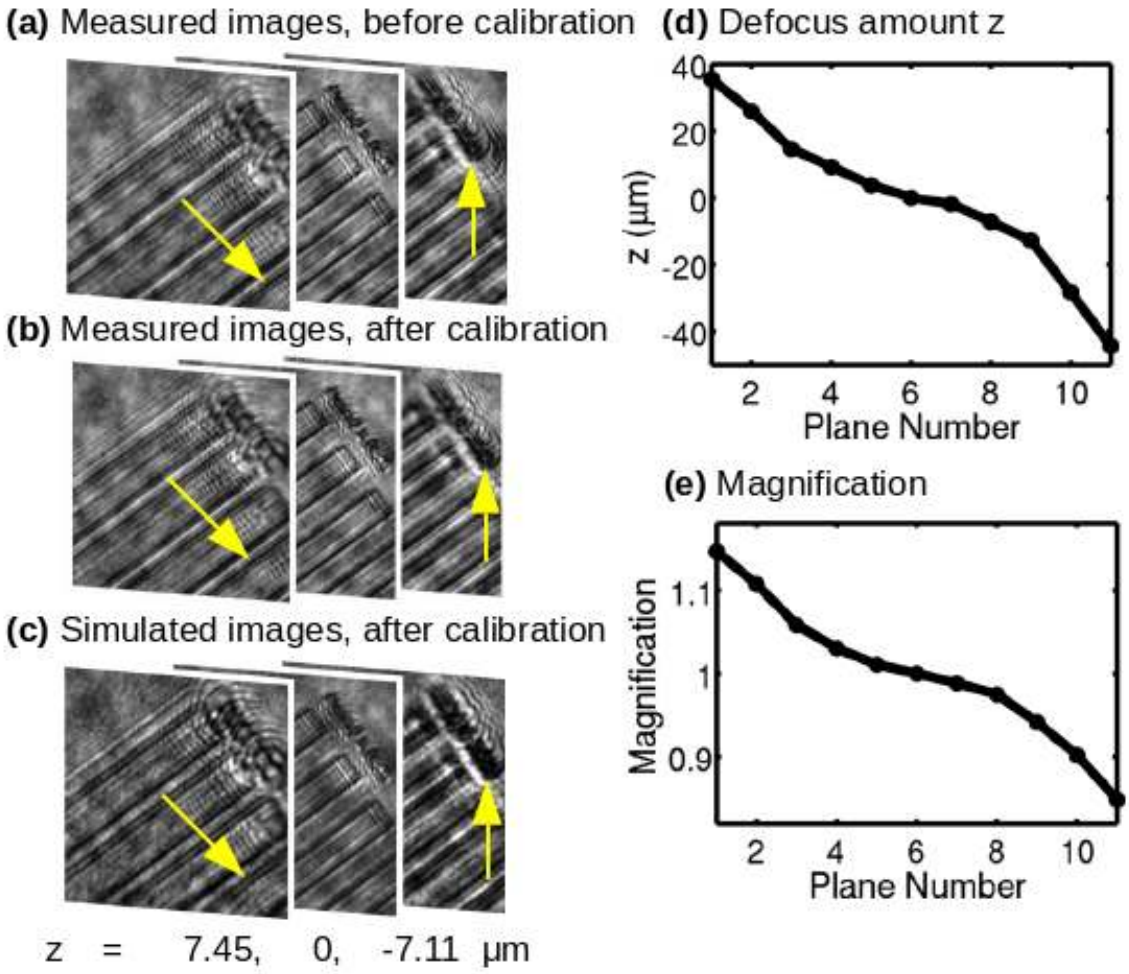

Fig. 3.3. Images of a 12 μm period grating with $\theta = 12.7°$, before and after calibration. Note the measured and simulated images agree after calibration in (b) and (c). The yellow arrows highlight shifts which have been corrected.

to be the focal plane ($z = 0$). By design we choose the the plane spacing to increase non-linearly (approximately exponentially) in relation to the focal plane. We use the approximation that the amount of defocus is linearly related to the change in current applied to the ETL. The more closely spaced images capture high frequency variations in intensity, while images with more defocus contain low frequency information [63]. These images are constraints for an iterative phase retrieval algorithm [25, 26]. At each axial location, we compute an electric field with magnitude based on camera measurements and phase based on numerical propagation from the previous plane. This computation is iteratively repeated over each axial location to produce a phase which is consistent with our measurements.

After retrieving the phase for each angle of illumination, we combine the resulting complex electric fields (synthetic aperture imaging). Each field at oblique illumination highlights a portion of the spatial frequency domain not accessible by the DC field alone. We construct a synthesized spectrum $U_s(u, v)$ by first assigning the low frequencies (of radius approximately NA/λ) to be equal to the DC spectrum, denoted as $U_0(u, v)$. In other words, in partition 0 (Fig. 3.1(d)), $U_s(u, v) = U_0(u, v)$. When the beam is positioned at the periphery of the BFP (numbered as $1, \ldots, 4$ in Fig. 3.1(b)) let us denote the Fourier transform of the fields measured at these angles as $U_1(u, v), \ldots, U_4(u, v)$. Next we assign other partitions of $U_s(u, v)$ to corresponding spectra. For example, in partition 1 (Fig. 3.1(d)), $U_s(u, v) = U_1(u, v)$. Taking the inverse Fourier transform of $U_s(u, v)$, we can extract the synthesized phase [58].

3.3 Results

3.3.1 Phase Reconstruction of a 1 μm Grating

To demonstrate resolution enhancement, we first image a phase grating sample with a 1 μm period. In an earlier step (Fig. 3.3), we have determined the calibration parameters (lateral shifts, magnifications, and axial locations) by examining a different portion of the sample. The grating is patterned in PMMA film by electron beam

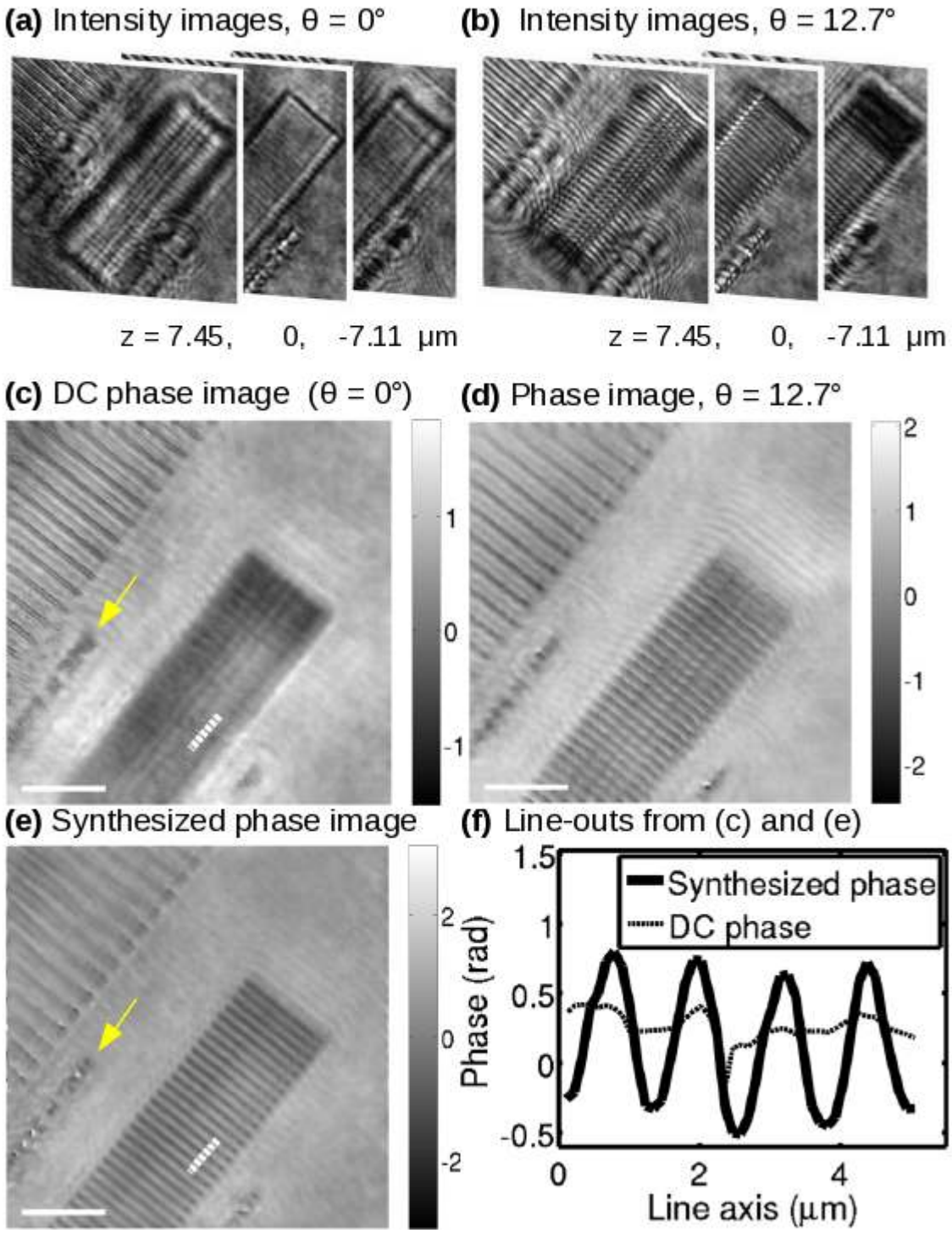

Fig. 3.4. Phase reconstruction of a grating sample with a 1 μm period (center grating). (c),(e) Yellow arrows highlight focusing dots which become more sharpened in (e). Scale bars: 8 μm.

lithography. Since the grating grooves lie below the planar surface of the PMMA film, we expect the grooves to have a shorter path length and hence appear darker than the background. The film thickness of 1.5 μm corresponds to a phase shift of $(2\pi/\lambda)\Delta n\Delta z - 2\pi \approx 1$ rad, where $\Delta n = 1.49 - 1 = 0.49$, $\Delta z = 1.5$ μm, $\lambda = 633$ nm, and we account for phase wrapping by subtracting 2π.

Figures 3.4(a) and (c) show some measured intensity images and the DC phase, respectively, in which the 1 μm grating pattern is indiscernible. Under oblique illumination the higher frequency pattern pops into view in Figs. 3.4(b) and (d) as a vivid demonstration of previously inaccessible frequency content. These angular fields enhance the resulting synthesized phase so that the pattern becomes clearly distinguishable in Fig. 3.4(e) and in the line-outs (Fig. 3.4(f)). The modulation depth of the grating in Fig. 3.4(f), measured by averaging the peak-to-valley heights in the synthesized phase line-out, is about 1 rad, which matches the expected phase shift given the PMMA film thickness of 1.5 μm.

3.3.2 Phase Reconstruction of a Biological Cell

Next we apply our technique to imaging cells, an important practical application. Fixed unstained cells from the Human Embryonic Kidney 293 (HEK-293) line serve as our sample of interest. For calibration, we examine a portion of the sample to correct for the lateral shifts. The magnifications and axial locations should be the same as determined from the phase grating. The lateral shifts differ because the beam travels through different material: PMMA film on glass substrate in one case, and a glass slide and phosphate buffered saline (PBS) medium in the other case. Once obtained, the calibration parameters apply to other samples made of the same materials.

A neuron-like cell from this sample, shown in Fig. 3.5(a), exhibits interesting phase features such as dendrites (labeled with arrows) and cellular structure, which we hope to better resolve. Using retrieved phases from multiple illumination angles, we construct the synthesized spectrum according to Fig. 3.1(d). The resulting syn-

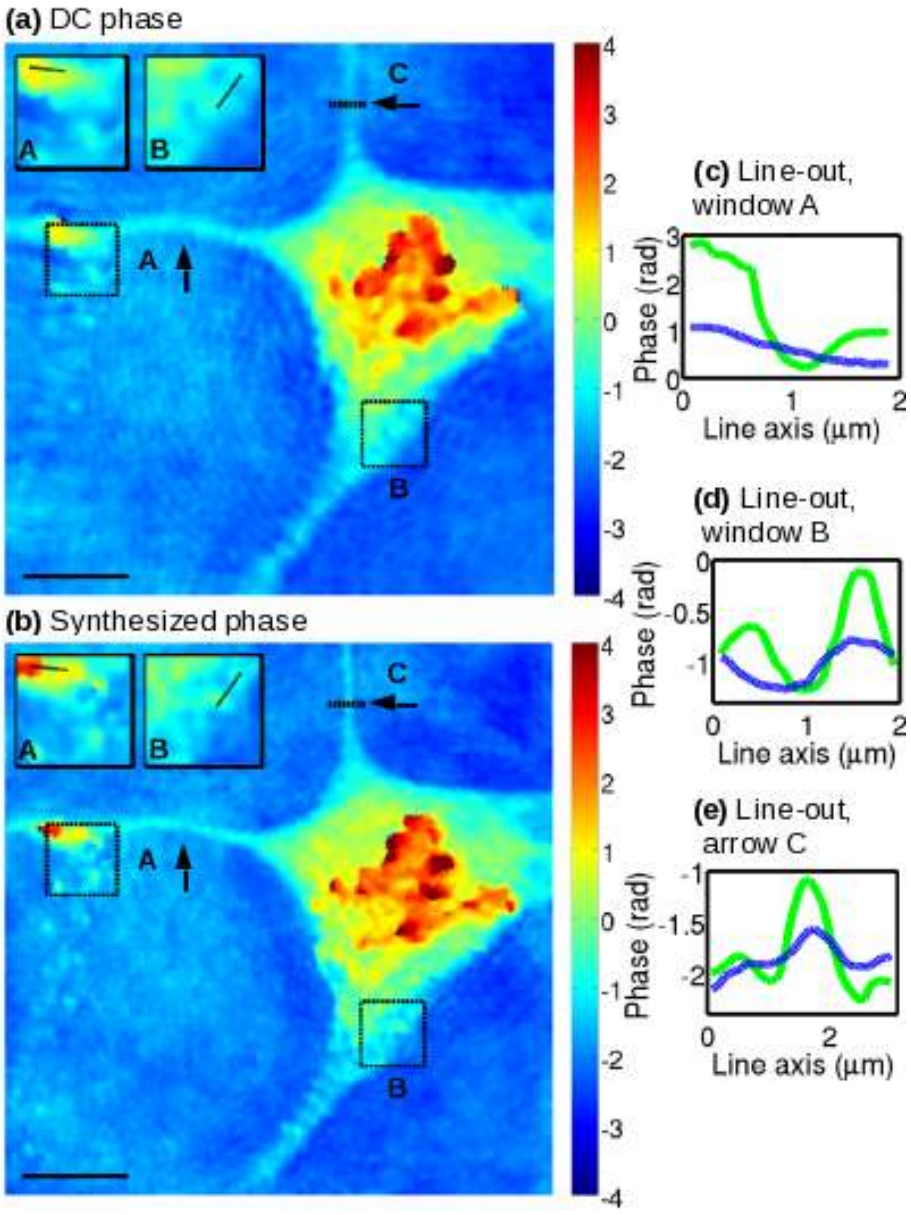

Fig. 3.5. Phase reconstruction of a HEK-293 cell. (c)-(e) Green line: synthesized phase, blue line: DC phase. Scale bars: 8 μm.

thesized phase displays features enhanced in resolution. To aid visualization, boxes A and B in Figs. 3.5(a) and (b) highlight phase enhancements with the corresponding line-outs plotted in Figs. 3.5(c) and (d). In particular, an axon terminal becomes more visible in box A. Additionally, the dendrites, labeled with arrows, show more clearly defined profiles in the synthesized phase.

To quantify the resolution improvement, we can first estimate the resolution before synthetic aperture imaging. In window B we see an example of two features which are barely resolvable in the DC phase but become distinguishable in the synthesized phase, as indicated by the line-out in Fig. 3.5(d). We estimate that these two features are separated by 1.2 μm, based on the green line (synthesized phase) in the line-out. Hence,

$$\delta = \frac{\kappa\lambda}{\mathrm{NA}} = 1.2\ \mu\mathrm{m}, \tag{3.19}$$

where κ is an experimental parameter that depends on factors like the signal to noise ratio of the detector, $\lambda = 633$ nm, and NA $= 0.75$. After synthetic aperture imaging, NA improves to NA $+ \sin\theta_{\mathrm{illum}} = 0.97$, and the resolution improves to

$$\delta = \frac{\kappa\lambda}{\mathrm{NA} + \sin\theta_{\mathrm{illum}}} = 0.9\ \mu\mathrm{m}, \tag{3.20}$$

where $\theta_{\mathrm{illum}} = 12.7^\circ$ is the largest angle of illumination used in our experiment. This value makes sense since we are able to resolve the 1 μm grating in the synthesized phase, as shown by the line-out in Fig. 3.4(f).

3.4 Conclusion

We have demonstrated synthetic aperture microscopy based on referenceless phase retrieval with an electrically tunable lens. The ETL is a compact, relatively low cost device, in contrast to other defocusing mechanisms such as a moving translation stage or 2D SLM. We have devised a calibration algorithm to register and rescale images and compute the axial locations of image planes. The developed algorithm is more generaly useful for applications that are sensitive to image alignment, scaling, or defocus, and it may enable other applications to benefit from the use of an ETL.

4. SINGLE SHOT DIGITAL HOLOGRAPHY BASED ON ITERATIVE RECONSTRUCTION WITH ALTERNATING UPDATES OF AMPLITUDE AND PHASE

In this work, we propose a new technique to recover high quality images in single shot digital holography. We develop an iterative reconstruction algorithm based on alternating updates of amplitude and phase. Unlike the standard Fourier filtering computation, our method is not constrained by finite filter window size. In addition, this alternating update strategy allows prior knowledge such as object smoothness to be applied to amplitude and phase separately. Regularizing phase separately helps to mitigate effects of poor signal-to-noise ratio caused by low signal amplitude. We demonstrate the effectiveness of our technique on simulated and experimentally measured data.

4.1 Introduction

Digital holography has many versatile applications, including microscopy [9, 15], phase contrast [13, 64], 3D displays [65], tomography [17], and terahertz imaging [66]. This technique enables the measurement of both amplitude and phase, which is especially useful for quantifying path lengths, measuring index contrast, or viewing biological samples [9, 58]. The complex object field, which is comprised of amplitude and phase, can be extracted from a hologram in different ways. In phase-shifting interferometry, the phase of the reference wave is stepped in increments; common increments are 0, $\pi/2$, π, and $3\pi/2$ [14]. The phase image is then extracted from the images measured at each step. However, this method requires multiple images to be recorded on a vibration-free optical table, typically with expensive devices such as high frame rate cameras.

Off-axis interferometry enables the complex object field to be computed in a single shot. A common way to compute the object field from a hologram is to use spatial filtering in the frequency domain [44, 67]. However, spatial filtering has some drawbacks. The zero order and cross terms have to be well-separated, and there is some subjectivity in choosing the filter window size. A variety of approaches have been proposed to help overcome this separation constraint between the zero order and cross terms. By suppressing the zero order term, these approaches aim to extend the spectral support of the image. Some examples of techniques include subracting the zero order term from the hologram [68], iteratively solving for the field in the spatial domain [69] and the frequency domain [70], and applying a nonlinear filter [71]. Other optimization-based approaches include formulating holography as a nonlinear least squares problem [72], as constrained optimization [73], as penalized likelihood with simulated data [74], or as a nonlinear inverse problem with total variation regularization [75].

In this work, we propose a new image reconstruction approach that recovers the complex object field from a single hologram frame. To overcome the limitations of choosing a finite window for Fourier filtering, we develop an iterative reconstruction algorithm based on alternating updates of amplitude and phase. In contrast, the state-of-the-art algorithms optimize with respect to the complex field [73–75]. The medical imaging literature discusses alternating updates for applications like magnetic resonance imaging [76]. To the best of our knowledge, this work is the first application of the alternating update strategy to single shot digital holography. Alternatively updating amplitude and phase has many advantages, enumerated below:

1. It allows prior knowledge on object constraints such as smoothness to be applied separately to amplitude and phase. For example, phase objects like transparent biological cells are smooth in amplitude, but it is desirable to preserve edges in phase.

2. It handles low amplitude areas in the image with poor signal. Since phase is weighted by amplitude in the complex field as $u = Ae^{i\phi}$, low amplitude areas will lead to a poor signal to noise ratio (SNR) in the phase image. Decoupling phase and amplitude allows the phase to be regularized separately.

3. Our implementation is able to regularize phase without requiring phase unwrapping. Other approaches assume that the phase is unwrapped before regularization [75].

4. Experimentally we find that this alternating update strategy results in better convergence than only updating the complex object field.

This work is organized as follows. In Section 4.2, we formulate the problem as a minimization of a cost function to solve for amplitude and phase. We present our algorithm in Section 4.2.4. We will compare our technique with standard Fourier filtering and another algorithm from Section 4.2.5. In Section 4.3, we test our method on simulated and experimental data. Finally in Section 4.4, we provide concluding remarks.

4.2 Theory

4.2.1 Continuous Formulation

In digital holography, an object field $o(\mathbf{x}) = A(\mathbf{x})e^{i\phi(\mathbf{x})}$ and a reference field $r(\mathbf{x}) = \tilde{A}(\mathbf{x})e^{i\tilde{\phi}(\mathbf{x})}$ combine to form an interference pattern measured on a camera:

$$\begin{aligned} I_{\text{ideal}}(\mathbf{x}) &= |o(\mathbf{x}) + r(\mathbf{x})|^2 \\ &= \left|A(\mathbf{x})e^{i\phi(\mathbf{x})} + \tilde{A}(\mathbf{x})e^{i\tilde{\phi}(\mathbf{x})}\right|^2 \\ &= A^2(\mathbf{x}) + \tilde{A}^2(\mathbf{x}) + 2A(\mathbf{x})\tilde{A}(\mathbf{x})\cos\left(\phi(\mathbf{x}) - \tilde{\phi}(\mathbf{x})\right) \end{aligned} \tag{4.1}$$

where $\mathbf{x} = (x_1, x_2)$ is the spatial coordinate in the camera plane. The measured hologram is generally noisy, which we can model as Gaussian noise that corrupts the interference pattern $I_{\text{ideal}}(\mathbf{x})$. Let $I(\mathbf{x})$ denote the measured hologram. It is also

possible to model the measured hologram using a Poisson distribution [77, 78]. We formulate the problem as the minimization of a cost function with general form

$$c(A,\phi) = L(A,\phi) + \beta_A R(A) + \beta_\phi R(\phi)$$

where $L(A,\phi)$ is the negative log-likelihood function corresponding to our model of the noisy hologram as a Gaussian distribution, β_A and β_ϕ are scalar regularization parameters, and $R(A)$ and $R(\phi)$ are roughness penalty functions for amplitude and phase, respectively. In the continuous formulation, the likelihood function has the form

$$L(A,\phi) = \int_{\mathbb{R}^2} \left[A^2(\mathbf{x}) + \tilde{A}^2(\mathbf{x}) + 2A(\mathbf{x})\tilde{A}(\mathbf{x})\cos\left(\phi(\mathbf{x}) - \tilde{\phi}(\mathbf{x})\right) - I(\mathbf{x})\right]^2 d\mathbf{x}. \quad (4.2)$$

To reduce noise and impose prior knowledge such as edge-preserving smoothness on the object, we also minimize the total variation of the amplitude and phase with the regularizer terms

$$R(A) = \int_{\mathbb{R}^2} \sqrt{|\nabla A(\mathbf{x})|^2 + \epsilon}\; d\mathbf{x}, \quad (4.3)$$

$$R(\phi) = \int_{\mathbb{R}^2} \sqrt{|\nabla e^{i\phi(\mathbf{x})}|^2 + \epsilon}\; d\mathbf{x} \quad (4.4)$$

where ϵ is a small constant to ensure differentiability. Other prior models can also be used [79]. Now the cost function becomes

$$\begin{aligned} c(A,\phi) &= L(A,\phi) + \beta_A R(A) + \beta_\phi R(\phi) \\ &= \int_{\mathbb{R}^2} \left[A^2(\mathbf{x}) + \tilde{A}^2(\mathbf{x}) + 2A(\mathbf{x})\tilde{A}(\mathbf{x})\cos\left(\phi(\mathbf{x}) - \tilde{\phi}(\mathbf{x})\right) - I(\mathbf{x})\right]^2 d\mathbf{x} \\ &\quad + \beta_A \int_{\mathbb{R}^2} \sqrt{|\nabla A(\mathbf{x})|^2 + \epsilon}\; d\mathbf{x} + \beta_\phi \int_{\mathbb{R}^2} \sqrt{|\nabla e^{i\phi(\mathbf{x})}|^2 + \epsilon}\; d\mathbf{x}. \end{aligned} \quad (4.5)$$

Our goal is to solve for amplitude and phase by minimizing this cost function:

$$\left(\hat{A}, \hat{\phi}\right) = \underset{A,\phi}{\operatorname{argmin}}\, c(A,\phi). \quad (4.6)$$

4.2.2 Discrete Formulation

According to the pixel pitch Δ_x of the camera, we can write the sampled likelihood function as

$$\begin{aligned} L(A,\phi) &= \sum_{\mathbf{m}\in\mathbb{Z}^2} \left[A^2(\mathbf{x}) + \tilde{A}^2(\mathbf{x}) + 2A(\mathbf{x})\tilde{A}(\mathbf{x})\cos\left(\phi(\mathbf{x}) - \tilde{\phi}(\mathbf{x})\right) - I(\mathbf{x})\right]^2 \Bigg|_{\mathbf{x}=\mathbf{m}\Delta_x} \\ &= \sum_i \left[\mathbf{A}_i^2 + \tilde{\mathbf{A}}_i^2 + 2\mathbf{A}_i\tilde{\mathbf{A}}_i\cos\left(\boldsymbol{\phi}_i - \tilde{\boldsymbol{\phi}}_i\right) - \mathbf{I}_i\right]^2 \end{aligned} \tag{4.7}$$

where $\mathbf{A}$ and $\tilde{\mathbf{A}}$ are vectors of the sampled object and reference amplitudes respectively, where pixels are arranged in raster scan order. Similarly, $\mathbf{I}$, ϕ, and $\tilde{\phi}$ are vectors of the sampled interference pattern and the object and reference phases respectively. A subscript such as $\mathbf{A}_i$ refers to the ith element of the vector. The regularizer functions are written as

$$R(\mathbf{A}) = \sum_i \sqrt{(\mathbf{C}\mathbf{A})_i^2 + \epsilon}, \tag{4.8}$$

$$R(\boldsymbol{\phi}) = \sum_i \sqrt{|\mathbf{C}e^{i\boldsymbol{\phi}}|_i^2 + \epsilon} \tag{4.9}$$

where $\mathbf{C}$ is a convolution matrix implementing the discretized first derivatives of the nearest neighbors. For example, in

$$\mathbf{C} = \begin{bmatrix} \mathbf{C}_h & \mathbf{C}_v \end{bmatrix}^T, \tag{4.10}$$

$\mathbf{C}$ is a concatenation of $\mathbf{C}_h$ and $\mathbf{C}_v$ which implements first derivatives in the horizonal and vertical directions respectively. Since we are examining derivatives of $e^{i\boldsymbol{\phi}}$, no phase unwrapping is required for regularization. The cost function becomes

$$\begin{aligned} c(\mathbf{A},\boldsymbol{\phi}) &= L(\mathbf{A},\boldsymbol{\phi}) + \beta_A R(\mathbf{A}) + \beta_\phi R(\boldsymbol{\phi}) \\ &= \sum_i \left[\mathbf{A}_i^2 + \tilde{\mathbf{A}}_i^2 + 2\mathbf{A}_i\tilde{\mathbf{A}}_i\cos\left(\boldsymbol{\phi}_i - \tilde{\boldsymbol{\phi}}_i\right) - \mathbf{I}_i\right]^2 \\ &\quad + \beta_A \sum_i \sqrt{(\mathbf{C}\mathbf{A})_i^2 + \epsilon} + \beta_\phi \sum_i \sqrt{|\mathbf{C}e^{i\boldsymbol{\phi}}|_i^2 + \epsilon}. \end{aligned} \tag{4.11}$$

Our goal is to solve for $\mathbf{A}$ and ϕ by minimizing this cost function:

$$\left(\hat{\mathbf{A}}, \hat{\boldsymbol{\phi}}\right) = \underset{\mathbf{A}, \boldsymbol{\phi} \in \mathbb{R}^N}{\operatorname{argmin}} c(\mathbf{A}, \boldsymbol{\phi}). \tag{4.12}$$

We estimate $\mathbf{A}$ and $\boldsymbol{\phi}$ by alternatively updating them in each iteration:

$$\mathbf{A}^{(n+1)} = \underset{\mathbf{A} \in \mathbb{R}^N}{\operatorname{argmin}} c(\mathbf{A}, \boldsymbol{\phi}^{(n)}), \tag{4.13}$$

$$\boldsymbol{\phi}^{(n+1)} = \underset{\boldsymbol{\phi} \in \mathbb{R}^N}{\operatorname{argmin}} c(\mathbf{A}^{(n+1)}, \boldsymbol{\phi}). \tag{4.14}$$

4.2.3 Alternative Formulation: Solve for the Complex Object Field

The interference pattern can be written in terms of amplitude and phase as in Eq. (4.1), or it can be written in terms of the reference and object fields:

$$I_{\text{ideal}}(\mathbf{x}) = |r(\mathbf{x})|^2 + |o(\mathbf{x})|^2 + o(\mathbf{x})r^*(\mathbf{x}) + o^*(\mathbf{x})r(\mathbf{x}). \tag{4.15}$$

As before, let $I(\mathbf{x})$ denote the measured hologram. An alternative formulation of the problem is to minimize a cost function in terms of the complex object field:

$$c(\mathbf{o}) = L(\mathbf{o}) + \beta R(\mathbf{o})$$

where β is a scalar regularization parameter. The likelihood function is

$$L(\mathbf{o}) = \sum_i \left[|\mathbf{r}_i|^2 + |\mathbf{o}_i|^2 + \mathbf{o}_i \mathbf{r}_i^* + \mathbf{o}_i^* \mathbf{r}_i - \mathbf{I}_i \right]^2 \tag{4.16}$$

where $\mathbf{o}$ and $\mathbf{r}$ are vectors of the sampled complex object and reference fields. We also minimize the total variation of the object field with the regularizer term

$$R(\mathbf{o}) = \sum_i \sqrt{|\mathbf{C}\mathbf{o}|_i^2 + \epsilon}. \tag{4.17}$$

The cost function becomes

$$\begin{aligned} c(\mathbf{o}) &= L(\mathbf{o}) + \beta R(\mathbf{o}) \\ &= \sum_i \left[|\mathbf{r}_i|^2 + |\mathbf{o}_i|^2 + \mathbf{o}_i \mathbf{r}_i^* + \mathbf{o}_i^* \mathbf{r}_i - \mathbf{I}_i \right]^2 + \beta \sum_i \sqrt{|\mathbf{C}\mathbf{o}|_i^2 + \epsilon}. \end{aligned} \tag{4.18}$$

For comparison with optimization based on alternating updates of amplitude and phase, our goal is to solve for the complex object field by minimizing this cost function:

$$\mathbf{o} = \underset{\mathbf{o} \in \mathbb{C}^N}{\operatorname{argmin}} c(\mathbf{o}). \tag{4.19}$$

4.2.4 Optimization Algorithm Based on Alternating Updates

We solve the problem of Eqs. (4.12)-(4.14) by alternatively updating $\mathbf{A}$ and ϕ in each iteration of an outer loop. We use two inner loops: one to update $\mathbf{A}$ and another to update ϕ. Each inner loop uses gradient descent to minimize the cost function in Eq. (4.11). We use the following iterative algorithm:

1. Initialize $\mathbf{A}$, $\boldsymbol{\phi}$, for example, by Fourier filtering.

2. Solve for $\mathbf{A}^{(n+1)} = \text{argmin}_{\mathbf{A}\in\mathbb{R}^N} c\left(\mathbf{A}, \boldsymbol{\phi}^{(n)}\right)$.

   (a) We compute $\mathbf{A}^{(n+1)}$ in an inner loop. Let $\mathbf{A}^{(n,i)}$ denote the nth and ith iterations of the outer and inner loops respectively. Initialize $\mathbf{A}^{(n,0)} \leftarrow \mathbf{A}^{(n)}$. Compute the cost gradient:

   $$\mathbf{d} = \left.\nabla_{\mathbf{A}} c\left(\mathbf{A}, \boldsymbol{\phi}^{(n)}\right)\right|_{\mathbf{A}=\mathbf{A}^{(n,i)}} = \left.\nabla_{\mathbf{A}} L\left(\mathbf{A}, \boldsymbol{\phi}^{(n)}\right)\right|_{\mathbf{A}=\mathbf{A}^{(n,i)}} + \beta_A \left.\nabla_{\mathbf{A}} R(\mathbf{A})\right|_{\mathbf{A}=\mathbf{A}^{(n,i)}}. \tag{4.20}$$

   (b) Perform a line search to find the optimal step size α^*:

   $$\alpha^* = \underset{\alpha}{\text{argmin}}\, c\left(\mathbf{A}^{(n,i)} + \alpha\mathbf{d}, \boldsymbol{\phi}^{(n)}\right). \tag{4.21}$$

   (c) Set

   $$\mathbf{A}^{(n,i+1)} \leftarrow \mathbf{A}^{(n,i)} + \alpha^*\mathbf{d}, \tag{4.22}$$

   $$i \leftarrow i + 1. \tag{4.23}$$

   Return to step (a) and repeat for desired number of iterations or until cost $c\left(\mathbf{A}, \boldsymbol{\phi}\right)$ is below a specified threshold. After the inner loop is finished, set

   $$\mathbf{A}^{(n+1)} \leftarrow \mathbf{A}^{(n,i)}. \tag{4.24}$$

3. Solve for $\boldsymbol{\phi}^{(n+1)} = \text{argmin}_{\boldsymbol{\phi}\in\mathbb{R}^N} c\left(\mathbf{A}^{(n+1)}, \boldsymbol{\phi}\right)$.

(a) We compute $\boldsymbol{\phi}^{(n+1)}$ in an inner loop. Let $\boldsymbol{\phi}^{(n,i)}$ denote the nth and ith iterations of the outer and inner loops respectively. Initialize $\boldsymbol{\phi}^{(n,0)} \leftarrow \boldsymbol{\phi}^{(n)}$. Compute the cost gradient:

$$\mathbf{d} = \left.\nabla_{\boldsymbol{\phi}} c\left(\mathbf{A}^{(n+1)}, \boldsymbol{\phi}\right)\right|_{\boldsymbol{\phi}=\boldsymbol{\phi}^{(n,i)}} = \left.\nabla_{\boldsymbol{\phi}} L\left(\mathbf{A}^{(n+1)}, \boldsymbol{\phi}\right)\right|_{\boldsymbol{\phi}=\boldsymbol{\phi}^{(n,i)}} + \beta_{\phi} \left.\nabla_{\boldsymbol{\phi}} R(\boldsymbol{\phi})\right|_{\boldsymbol{\phi}=\boldsymbol{\phi}^{(n,i)}}. \tag{4.25}$$

(b) Perform a line search to find the optimal step size α^*:

$$\alpha^* = \underset{\alpha}{\operatorname{argmin}}\, c\left(\mathbf{A}^{(n+1)}, \boldsymbol{\phi}^{(n,i)} + \alpha \mathbf{d}\right). \tag{4.26}$$

(c) Set

$$\boldsymbol{\phi}^{(n,i+1)} \leftarrow \boldsymbol{\phi}^{(n,i)} + \alpha^* \mathbf{d}, \tag{4.27}$$

$$i \leftarrow i + 1. \tag{4.28}$$

Return to step (a) and repeat for desired number of iterations or until cost $c\left(\mathbf{A}, \boldsymbol{\phi}\right)$ is below a specified threshold. After the inner loop is finished, set

$$\boldsymbol{\phi}^{(n+1)} \leftarrow \boldsymbol{\phi}^{(n,i)}. \tag{4.29}$$

4. Set

$$n \leftarrow n + 1. \tag{4.30}$$

Return to step 2 and repeat for desired number of iterations or until cost $c\left(\mathbf{A}, \boldsymbol{\phi}\right)$ is below a specified threshold.

Note that the cost gradients in Eqs. (4.20) and (4.25) involves calculating the gradients $\nabla_{\mathbf{A}} L(\mathbf{A}, \boldsymbol{\phi})$ and $\nabla_{\boldsymbol{\phi}} L(\mathbf{A}, \boldsymbol{\phi})$. For reference, the expressions for these gradients are listed in Appendix A.

Since the cost function in Eq. (4.11) is non-convex [80], the algorithm may converge to a local minimum depending on the initial guess for $\mathbf{A}$ and $\boldsymbol{\phi}$. For example, we can compute the initial guess by using Fourier filtering. Alternatively, as an initial guess, we can use the output of another algorithm based on minimizing cost with respect to the complex object field; this algorithm is discussed later. Empirically, we find that these two ways of initialization yield good convergence.

4.2.5 Optimization Algorithm to Solve for the Complex Object Field

Instead of minimizing over amplitude and phase, we can try to minimize over the complex object field by solving the problem in Eq. (4.19). In this case, we use only one loop for iteratively minimizing the cost by gradient descent. The algorithm proceeds as follows:

1. Initialize $\mathbf{o}$, for example, by Fourier filtering.

2. Compute the cost gradient

$$\mathbf{d} = \left.\nabla_{\mathbf{o}} c\left(\mathbf{o}\right)\right|_{\mathbf{o}=\mathbf{o}^{(n)}} = \left.\nabla_{\mathbf{o}} L\left(\mathbf{o}\right)\right|_{\mathbf{o}=\mathbf{o}^{(n)}} + \beta \left.\nabla_{\mathbf{o}} R(\mathbf{o})\right|_{\mathbf{o}=\mathbf{o}^{(n)}}. \tag{4.31}$$

3. Perform a line search to find the optimal step size α^*:

$$\alpha^* = \underset{\alpha}{\operatorname{argmin}}\, c\left(\mathbf{o}^{(n)} + \alpha \mathbf{d}\right). \tag{4.32}$$

4. Set

$$\mathbf{o}^{(n+1)} \leftarrow \mathbf{o}^{(n)} + \alpha^* \mathbf{d}, \tag{4.33}$$

$$n \leftarrow n + 1. \tag{4.34}$$

   Return to step 2 and repeat for desired number of iterations or until cost $c(\mathbf{o})$ is below a specified threshold.

Note that computing the cost gradient in Eq. (4.31) depends on the quantity $\nabla_{\mathbf{o}} L(\mathbf{o})$. For reference, we list this quantity in Appendix A. Empirically, we find that making an initial guess by Fourier filtering or by guessing a zero image yields good convergence. Note that the current literature discusses variants of this strategy of minimizing over the complex object field. As outlined in Section 4.1, our algorithm based on alternating updates of amplitude and phase offers advantages over the current techniques.

4.3 Experiment

We test our iterative reconstruction algorithm on both simulated and experimentally measured data. We will compare our technique with standard Fourier filtering

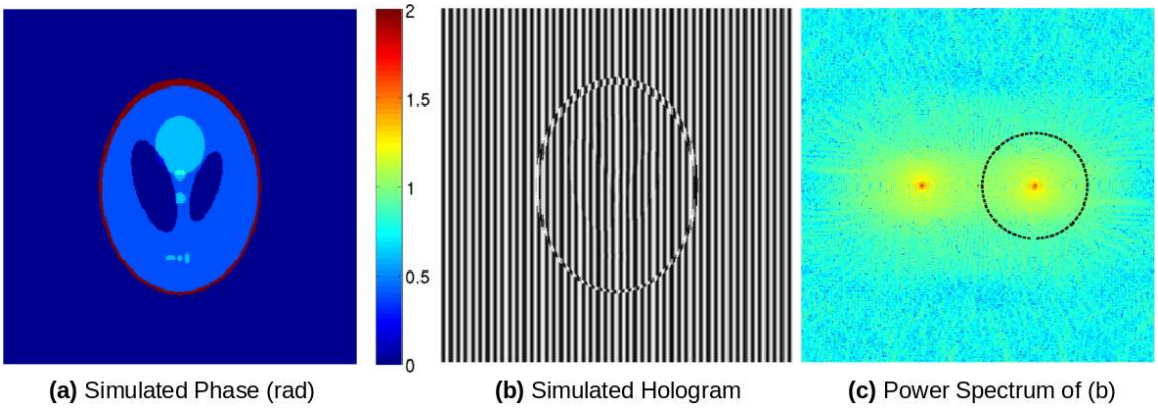

Fig. 4.1. Illustration of limited filter window size on a simulated phantom. (a) Simulated phase image (rad). (b) Simulated hologram corresponding to (a). (c) Power spectrum of (b).

and with an algorithm based on solving for the complex object field. Our goal is to demonstrate the advantages outlined in Section 4.1.

4.3.1 Simulated Data

For simulation, we create a test object consisting of uniform amplitude $A(\mathbf{x})$ equal to 1 everywhere. We set the phase $\boldsymbol{\phi}(\mathbf{x})$ to have the form of the Shepp-Logan phantom, as shown in Fig. 4.1(a). The resulting object $o(\mathbf{x}) = e^{i\phi(\mathbf{x})}$. To simulate an off-axis configuration, the reference beam is $r(\mathbf{x}) = e^{i2\pi\mathbf{f}\cdot\mathbf{x}}$. We choose $|\mathbf{f}| = (0.16, 0)$, where frequency has units of $(\text{pixel})^{-1}$. For demonstration, $|\mathbf{f}|$ is set to be small enough so that the zero order and cross terms overlap in the frequency domain. The corresponding interference pattern is shown in Fig. 4.1(b), with its Fourier transform in Fig. 4.1(c). A common way of extracting $\phi(\mathbf{x})$ is to apply a filter in the frequency domain to select one of the sidebands. In Fig. 4.1(c), we indicate this filter with the black circle. This filter cannot be enlarged any further, otherwise it would encompass the DC frequency. Thus, a limitation of this technique is the finite window size, which may clip higher frequencies.

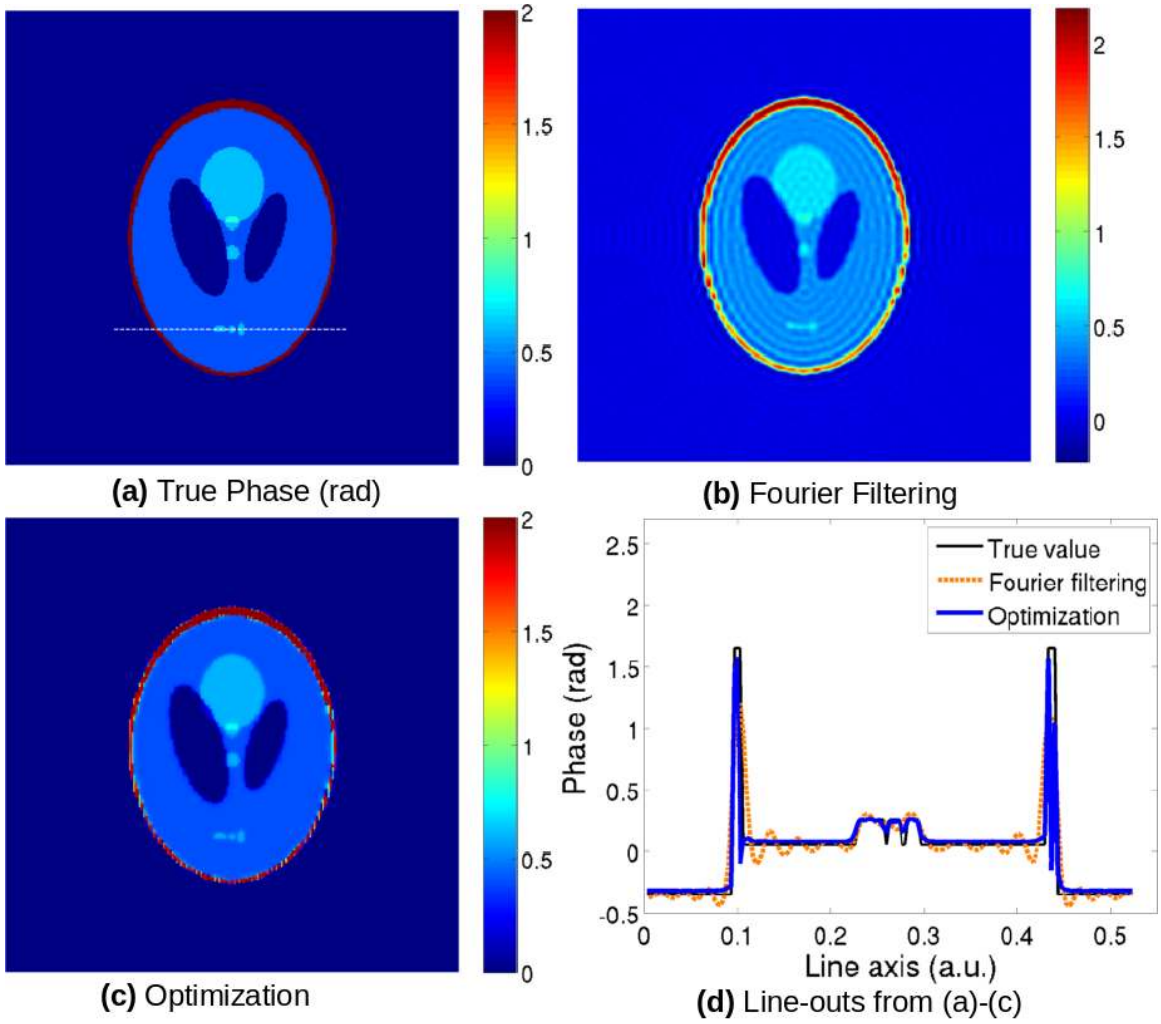

Fig. 4.2. Phase reconstruction of the simulated phantom. (a) True phase. (b) Phase from Fourier filtering (see Figs. 4.1(a)-(c)). (c) Phase from the proposed method (Section 4.2.4). (d) Line-out across the white dashed line in (a) with comparison to (b) and (c).

Table 4.1
Regularization Parameters Used for Simulated Data

	Proposed Method (Section 4.2.4)	Alternative Method (Section 4.2.5)
β_A	10	-
β_ϕ	0.5	-
β	-	100

Our algorithm helps to overcome this limitation of finite window size. As an illustration, we first retrieve phase by filtering in the frequency domain as shown in Fig. 4.1(c), and the computed phase is shown in Fig. 4.2(b). The test object has a high phase value of 2 rad at the outer edge, which contributes to the high frequency content in Fig. 4.1(c). Since the filter cuts off high frequencies, ringing occurs in the retrieved phase in Fig. 4.2(b). For comparison, we plot line-outs across the dashed white line in Fig. 4.2(a) and across the same points in Figs. 4.2(b) and (c). The line-out in Fig. 4.2(d) displays the ringing in the phase computed by Fourier filtering.

To compare with Fourier filtering, we compute phase by using our proposed algorithm from Section 4.2.4. Table 4.1 lists the regularization parameters. Figure 4.2(c) shows the resulting phase with the line-out plotted in Fig. 4.2(d) as the blue line labeled "Optimization." In contrast to the Fourier filtering result with ripple artifacts, the phase more closely matches the true value. In addition, the three dots in the phantom are now distinguishable.

Rather than alternating updates of amplitude and phase, we can directly solve for the complex object field. We apply the procedure in Section 4.2.5 on our simulated data and display the amplitude and phase in Figs. 4.3(a) and (b). Table 4.1 lists the regularization parameters. For comparison, the amplitude and phase from our proposed algorithm is shown in Figs. 4.3(c) and (d). Figure 4.3(b) shows residual modulation from the fringes and blurring of the 3 dots in the phantom. In Fig. 4.3(d), these fringe artifacts are reduced, and the 3 dots are distinguishable. In our technique,

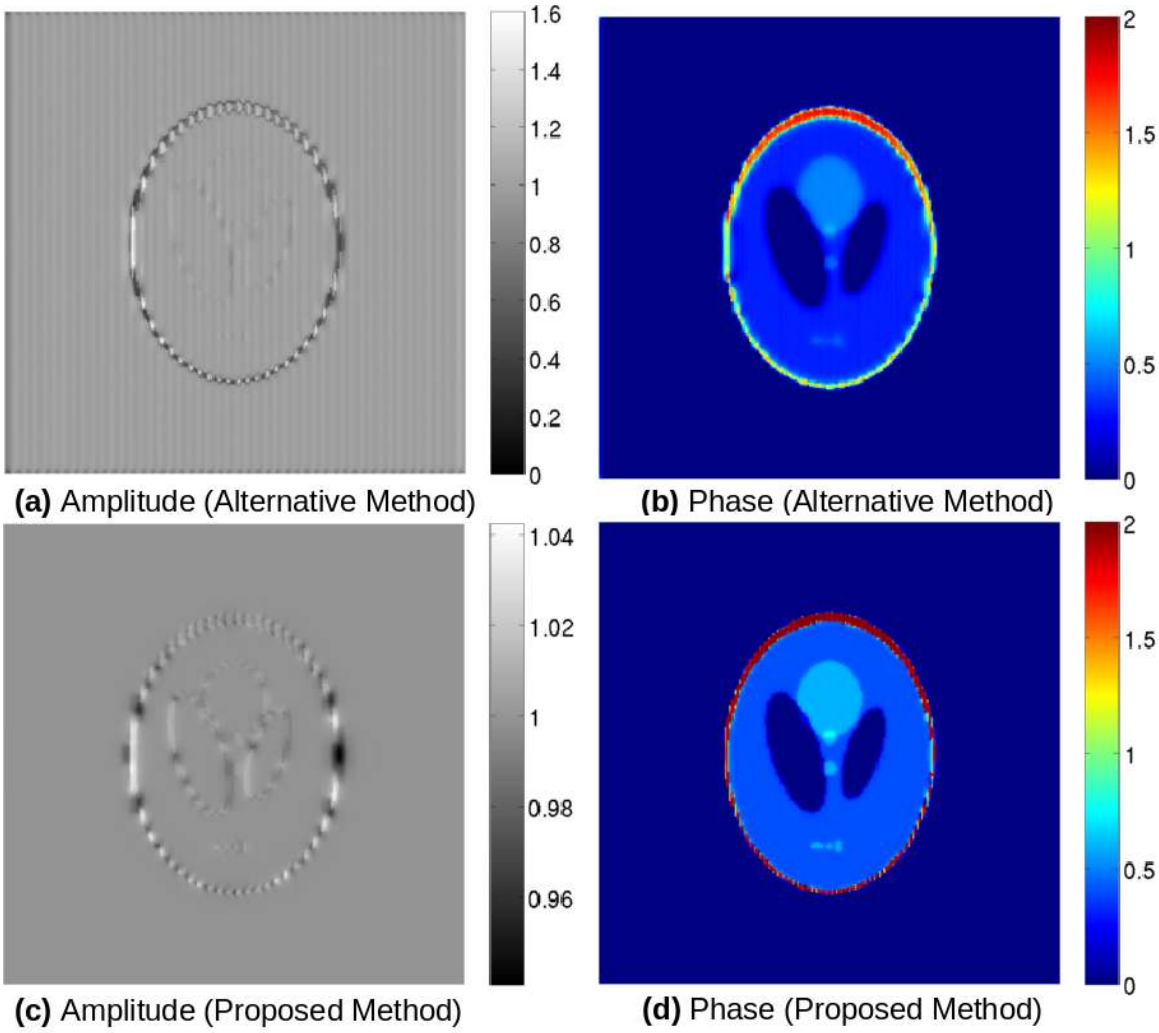

Fig. 4.3. Image reconstruction with two algorithms on simulated data. (a),(b) Reconstructed amplitude and phase using the alternative method (Section 4.2.5). (c),(d) Reconstructed amplitude and phase using the proposed method (Section 4.2.4). Note the change in grayscale between (a) and (c).

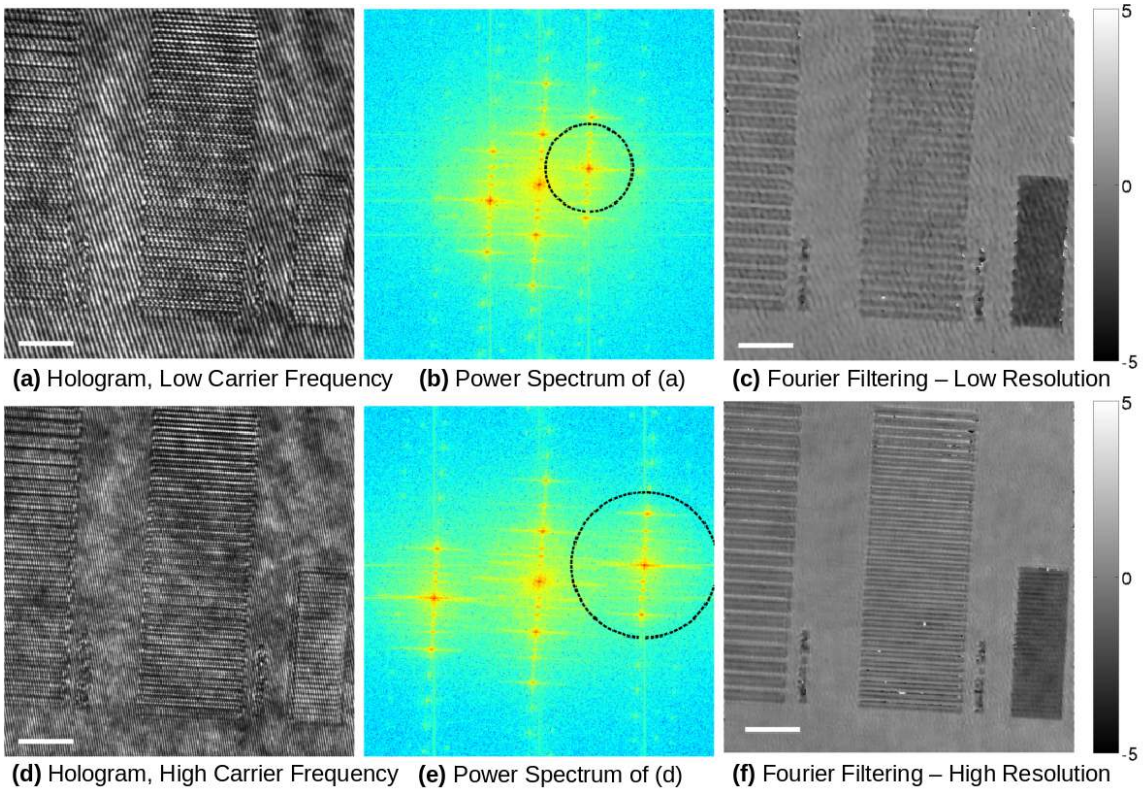

Fig. 4.4. Illustration of limited filter window size on experimental data. (a) Measured hologram with low carrier frequency. (b) Power spectrum of (a). (c) Phase from Fourier filtering with low carrier frequency. (d) Measured hologram with high carrier frequency. (e) Power spectrum of (d). (f) Phase from Fourier filtering with high carrier frequency. This serves as a reference or true phase. Scale bars = 10 μm.

we update amplitude and phase separately; it is more physically intuitive that each should be smooth, as opposed to enforcing that the modulus of the complex object field be smooth. The amplitude in Fig. 4.3(c) shows much less variation (about 0.09) than in Fig. 4.3(a) (about 1.6), since we are directly penalizing roughness on the amplitude in our algorithm from Section 4.2.4.

Table 4.2
Regularization Parameters Used for Experimental Data

	Proposed Method (Section 4.2.4)	Alternative Method (Section 4.2.5)
β_A	30	-
β_ϕ	50	-
β	-	20

4.3.2 Experimental Data

Next we test our proposed algorithm on experimentally measured data. Our sample consists of gratings patterned on PMMA film ($n = 1.49$) with a height contrast of about 1.5 μm. Using an off-axis configuration, we measure the hologram in Fig. 4.4(a) and take its Fourier transform in Fig. 4.4(b). First we try the Fourier filtering approach by applying a filter in the frequency domain, indicated by the black circle in Fig. 4.4(b). The resulting phase is shown in Fig. 4.4(c), which shows lower resolution due to the limited filter window size.

To obtain a reference or true phase, we measure phase with enhanced resolution by increasing the angle between object and reference beams. The carrier frequency increases, thus allowing the filter window size to increase. Figures 4.4(d)-(f) show the measured hologram, corresponding power spectrum with the applied filter circled in black, and retrieved phase at higher resolution. Although a high carrier frequency is ideal, sometimes the experimental configuration may not allow a large angle between object and reference beams, the geometry may be limited by other factors such as sampling requirements of the camera pixels, or the sample may contain high spatial frequencies. We will use the data at high carrier frequencies as a reference for our results. Our goal is to apply the proposed method (Section 4.2.4) to the low carrier frequency data (Fig. 4.4(a)).

We apply the proposed algorithm in Section 4.2.4 to our experimentally measured data (Fig. 4.4(a)), and the computed phase is shown in Fig. 4.5(c). Table 4.2 lists the

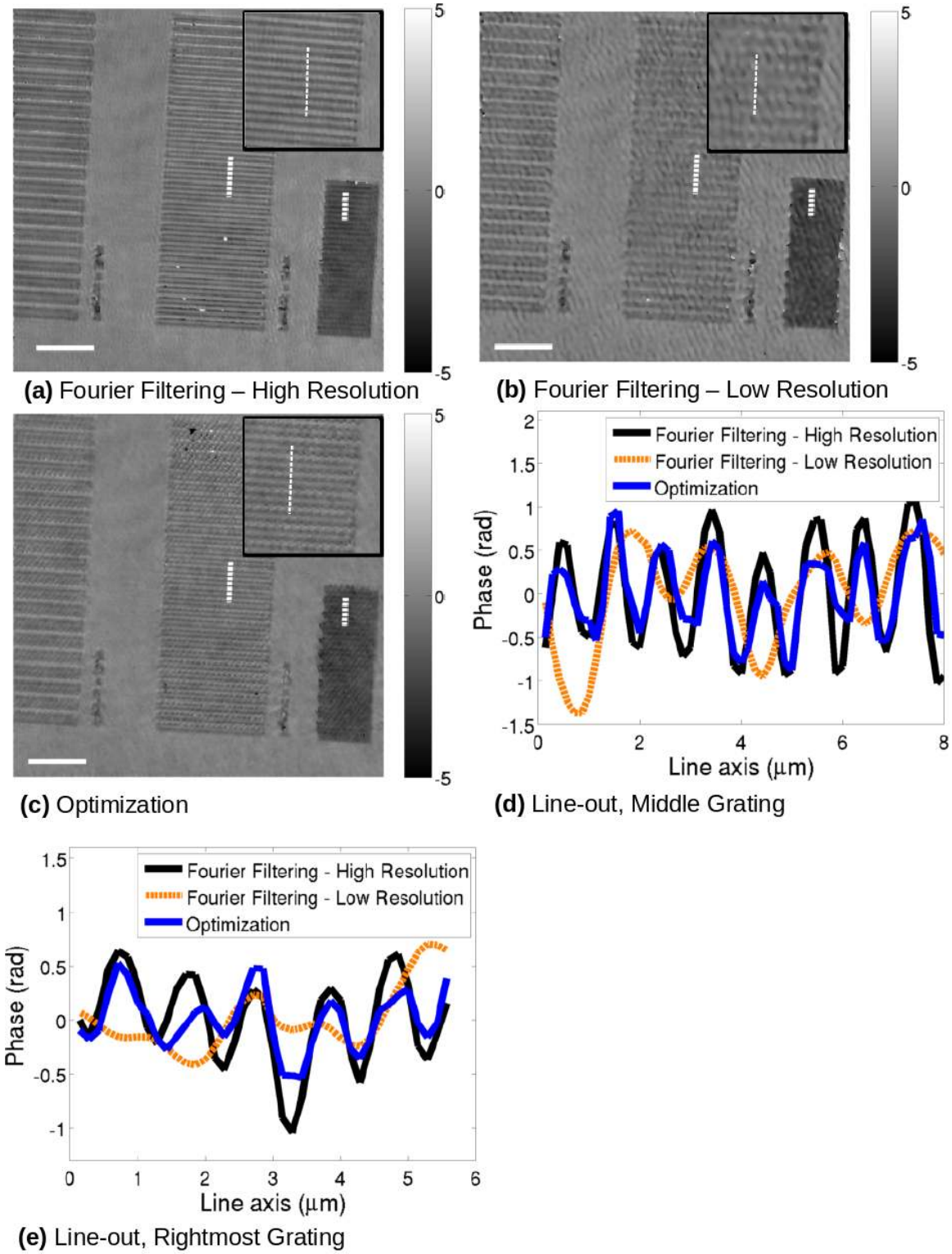

Fig. 4.5. Phase reconstruction of gratings. (a) Phase from Fourier filtering with high carrier frequency (see Figs. 4.4(d)-(f)). This serves as a reference or true phase. (b) Phase from Fourier filtering with low carrier frequency (see Figs. 4.4(a)-(c)). (c) Phase from the proposed method using low carrier frequency data. (d),(e) Line-outs across middle and rightmost gratings. Scale bars = 10 μm.

regularization parameters. In general Fig. 4.5(c) looks less noisy than Fig. 4.5(b). For display, the phase calculated by the algorithm is unwrapped; note a few unwrapping errors may be visible. Figure 4.5(d) shows a quantitative comparison of line-outs across the grating in the center of Figs. 4.5(a)-(c). This grating is designed to have a 2 μm period; due to diffraction effects, details that are finer than a 2 μm period appear. Using our proposed method, plotted as a blue line labeled "Optimization," we can see details from the diffraction features in the computed phase. Indeed the reference phase (black line) and our recovered phase (blue line) exhibit the same periodicity. Figure 4.5(e) plots line-outs across the grating on the rightmost side of Figs. 4.5(a)-(c). This grating is designed to have a 1 μm period. Fourier filtering results in loss of high frequency detail (orange line), but our algorithm recovers this detail as shown by the 1 μm period pattern in the line-out (blue line).

As with the simulated data, we can solve for the complex object field by applying the algorithm in Section 4.2.5. Table 4.2 lists the regularization parameters. Figures 4.6(a) and (b) show the amplitude and phase based on minimizing over the complex field, while Figs. 4.6(c) and (d) show the corresponding quantities using our proposed algorithm. The main difference is the loss of detail in Fig. 4.6(b) compared to the phase in Fig. 4.6(d). Part of the reason may be that the measured hologram in Fig. 4.4(a) has uneven illumination; areas of low SNR in the dark regions lead to poor phase reconstruction since phase is weighted by amplitude as $u = Ae^{i\phi}$. By separately updating $\mathbf{A}$ and $\boldsymbol{\phi}$, phase can be regularized independently from amplitude.

4.4 Conclusion

In this work we present an iterative reconstruction algorithm based on alternating updates of amplitude and phase for single shot digital holography. Through this approach, we are not subject to the limitations of the finite window size in Fourier filtering, and we can directly impose prior knowledge such as smoothness on amplitude and phase individually. Also, decoupling these two quantities allows phase to be

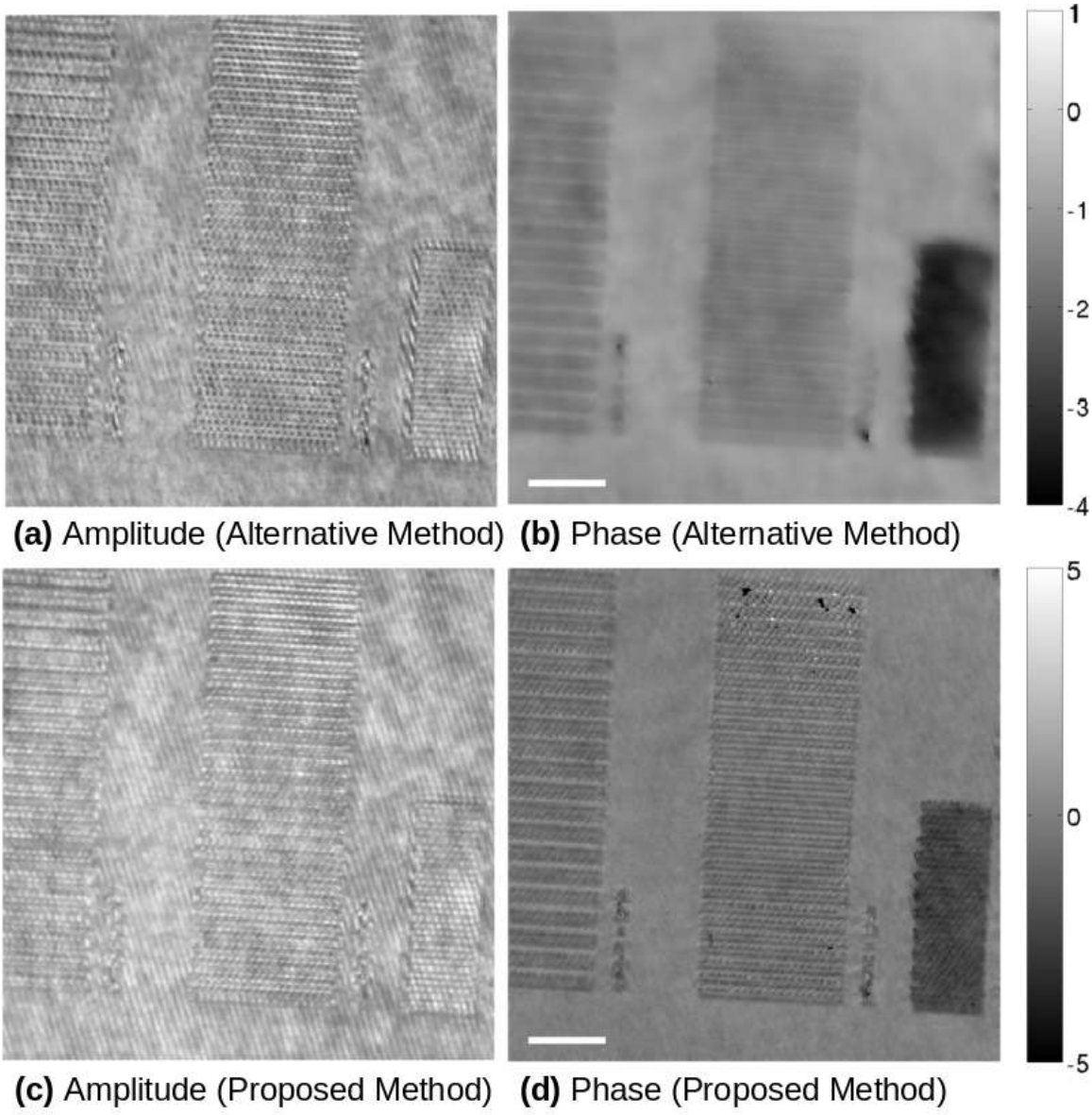

Fig. 4.6. Image reconstruction with two algorithms on experimental data. (a),(b) Reconstructed amplitude and phase using the alternative method (Section 4.2.5). (c),(d) Reconstructed amplitude and phase using the proposed method (Section 4.2.4). Scale bars = 10 μm.

regularized independently from amplitude, which helps to mitigate artifacts from low SNR. Note no phase unwrapping is required. This technique improves amplitude and phase reconstruction from measured single shot holograms, and it will benefit the many applications of digital holography.

5. SUMMARY AND FUTURE RESEARCH DIRECTIONS

5.1 Summary

In this work we experimentally and algorithmically investigate three main aspects of phase imaging microscopy including synthetic aperture imaging, phase retrieval, and digital holography. Chapter 1 summarizes the uses of phase imaging microscopy and some important problems in this field. In Chapter 2, we develop a microscope to enhance the resolution of phase images. Our non-holographic design offers the advantage of of being more stable than standard interferometric techniques, which are more sensitive to environmental vibrations and temperature fluctuations. By removing the reference arm, we achieve a more compact and less costly setup. We investigate phase measurements with a sample of 10 μm polystyrene beads and find our measurements to be in good agreement with holographic computations. We estimate our resolution to improve to 1.24 μm from 1.59 μm. To the best of our knowledge, this work is the first experimental demonstration of referenceless phase retrieval at off-axis illumination.

In Chapter 3, we implement a synthetic aperture microscope using an electrically tunable lens (ETL) for defocusing images. This design removes the need for mechanically moving the camera on a translation stage, and the ETL has the advantage of being a compact, low cost device. We develop a calibration algorithm for correcting for image shifts and magnifications and for quantifying defocus. The algorithm is more generally useful for applications that are sensitive to alignment and scaling of defocused images. We investigate the resolution enhancement of our technique by imaging a 1 μm grating patterned on PMMA film. The off-axis illumination enables us to see sub-μm resolution, with an increase in NA to 0.97 from 0.75. We also image a biological cell sample to illustrate the practical application of our technique. With

synthetic aperture imaging, we are able to resolve finer features in the cell. This work can potentially help other applications benefit from the use of an ETL.

In Chapter 4, we propose a new technique for reconstructing images from a digital hologram. Our iterative reconstruction algorithm is based on minimizing a cost function and alternatively updating amplitude and phase. The alternating update strategy applies prior knowledge such as object smoothness to amplitude and phase separately. The other alternative is to regularize the complex object field, but it is more physically intuitive to impose smoothness on the amplitude and phase separately. In addition, since low amplitudes multiply phase as $u = Ae^{i\phi}$, updating phase separately helps to decouple the effects of poor SNR on phase. For demonstration, we reconstruct phase from simulated data. The standard Fourier filtering computation suffers from ringing artifacts and loss of detail, while our technique shows improvement in these aspects. We also measure experimental data from a 1 μm grating patterned on PMMA film. The reconstructed phase shows an improvement in resolution and reduction in noise compared to Fourier filtering. To the best of our knowledge, this work is the first application and experimental demonstration of iterative reconstruction based on alternating updates of amplitude and phase to digital holography. Our technique can help improve image reconstruction for the many applications of digital holography.

5.2 Future Research Directions

In our research, we have measured 2D images of a sample at multiple angles for resolution enhancement. This idea is central to how tomography works [81]. Current techniques use some form of interferometry to implement tomographic phase microscopy. One interesting research direction is to apply our referenceless phase retrieval measurements to create a 3D tomogram of a sample. There are some challenges to implementing this experiment. One challenge is that phase retrieval may converge to a local minimum. There has been research in adding speckle modulation

to the diffracted light. The main idea is to make the low frequency parts of the image vary more rapidly through defocus. To leverage this idea, we can add speckle modulation to the images that we measure over all the angles. We can also use our calibration algorithm from Chapter 3 to register defocused images. We believe that studying tomographic imaging based on non-holographic implementations would be a useful contribution to phase microscopy.

Another interesting research direction is to stretch the alternating update approach of Chapter 4 to applications with partial data. For example, we can investigate image recovery as the hologram is downsampled [75] to see how our results compare with other algorithms. Our approach should be robust to sparse data since we can incorporate prior knowledge such as piecewise smoothness in our cost function. Downsampling the hologram is a useful application since it would speed data acquisition times. Another practical application is dealing with low light or high noise. We could extend our experiment to vary illumination levels; ideally we should still be able to reconstruct amplitude and phase with our technique. It would be interesting to compare the noise performance of our algorithm with other methods.

LIST OF REFERENCES

LIST OF REFERENCES

[1] B. Huang, M. Bates, and X. Zhuang, "Super-resolution fluorescence microscopy," Annu. Rev. Biochem. **78**, 993 (2009).

[2] J. A. Rodrigo, T. Alieva, G. Cristbal, and M. L. Calvo, "Wavefield imaging via iterative retrieval based on phase modulation diversity," Opt. Express **19**, 18621-18635 (2011).

[3] J. W. Goodman, *Introduction to Fourier Optics* (McGraw-Hill, 1996).

[4] G. Popescu, *Quantitative Phase Imaging of Cells and Tissues* (McGraw-Hill, New York, 2011).

[5] H. G. Davies and M. H. F. Wilkins, "Interference microscopy and mass determination," Nature **169**, 541 (1952).

[6] B. Rappaz, P. Marquet, E. Cuche, Y. Emery, C. Depeursinge, and P. Magistretti, "Measurement of the integral refractive index and dynamic cell morphometry of living cells with digital holographic microscopy," Opt. Express **13**, 9361-9373 (2005).

[7] J. Wang, D. Lee, Y. Xuan, L. Fan, L. T. Varghese, P. Wang, D. E. Leaird, A. M. Weiner, and M. Qi, "Radio-Frequency Arbitrary Waveform Generation with a Programmable SiN Spectral Shaper," in CLEO: 2013, OSA Technical Digest (online) (Optical Society of America, 2013), paper CTu2G.4.

[8] P. Marquet, B. Rappaz, P. J. Magistretti, E. Cuche, Y. Emery, T. Colomb, and C. Depeursinge, "Digital holographic microscopy: a noninvasive contrast imaging technique allowing quantitative visualization of living cells with subwavelength axial accuracy," Opt. Lett. **30**, 468-470 (2005).

[9] G. Popescu, T. Ikeda, R. R. Dasari, and M. S. Feld, "Diffraction phase microscopy for quantifying cell structure and dynamics," Opt. Lett. **31**, 775-777(2006).

[10] A. Barty. K. A. Nugent, D. Paganin, and A. Roberts, "Quantitative optical phase microscopy," Opt. Lett. **23**, 817-819 (1998).

[11] M. Kim, Y. Choi, C. Fang-Yen, Y. Sung, K. Kim, R. R. Dasari, M. S. Feld, and W. Choi, "Three-dimensional differential interference contrast microscopy using synthetic aperture imaging," J. Biomed. Opt. **17**(2), 026003 (2012).

[12] U. Schnars, and W. Juptner, "Direct recording of holograms by a CCD target and numerical reconstruction," Appl. Opt. **33**(2), 179-181 (1994).

[13] E. Cuche, P. Marquet, and C. Depeursinge, "Simultaneous amplitude-contrast and quantitative phase-contrast microscopy by numerical reconstruction of Fresnel off-axis holograms," Appl. Opt. **38**, 6994-7001 (1999).

[14] I. Yamaguchi and T. Zhang, "Phase-shifting digital holography," Opt. Lett. **22**, 1268-1270 (1997).

[15] I. Yamaguchi, J. Kato, S. Ohta, and J. Mizuno, "Image formation in phase-shifting digital holography and applications to microscopy," Appl. Opt. **40**(34) 6177-6186 (2001).

[16] P. Gao, G. Pedrini, and W. Osten, "Structured illumination for resolution enhancement and autofocusing in digital holographic microscopy," Opt. Lett. **38**, 1328-1330 (2013).

[17] W. Choi, C. Fang-Yen, K. Badizadegan, S. Oh, N. Lue, R. R. Dasari, and M. S. Feld, "Tomographic phase microscopy," Nat. Methods **4**(9), 717-719 (2007).

[18] Y. Sung, W. Choi, C. Fang-Yen, K. Badizadegan, R. Dasari, and M. Feld, "Optical diffraction tomography for high resolution live cell imaging," Opt. Express **17**, 266-277 (2009).

[19] M. R. Teague, "Deterministic phase retrieval: a Green's function solution," J. Opt. Soc. Am. A **73**(11), 1434-1441 (1983).

[20] N. Streibl, "Phase imaging by the transport equation of intensity," Opt. Commun. **49**(1), 6-10 (1984).

[21] L. Allen and M. Oxley, "Phase retrieval from series of images obtained by defocus variation," Opt. Commun. **199**(1-4), 65-75 (2001).

[22] L. Waller, L. Tian, and G. Barbastathis, "Transport of intensity phase-amplitude imaging with higher-order intensity derivatives," Opt. Express **18**(12), 12552-12561 (2010).

[23] L. Waller, S. S. Kou, C. J. R. Sheppard, and G. Barbastathis, "Phase from chromatic aberrations," Opt. Express **18**(22), 22817-22825 (2010).

[24] R. W. Gerchberg, W. O. Saxton, "A practical algorithm for the determination of phase from image and diffraction plane pictures," Optik **35**, 227-246 (1972).

[25] J. R. Fienup, "Phase retrieval algorithms: a comparison," Appl. Opt. **21**, 2758-2769 (1982).

[26] G. Pedrini, W. Osten, and H. Tiziani, "Wave-front reconstruction from a sequence of interferograms recorded at different planes," Opt. Lett. **30**(8), 833-835(2005).

[27] P. Almoro, G. Pedrini, and W. Osten, "Complete wavefront reconstruction using sequential intensity measurements of a volume speckle field," Appl. Opt. **45**(34), 8596-8605 (2006).

[28] Y. Zhang, G. Pedrini, W. Osten, and H. Tiziani, "Whole optical wave field reconstruction from double or multi in-line holograms by phase retrieval algorithm," Opt. Express **11**, 3234-3241 (2003).

[29] P. Almoro and S. Hanson, "Wavefront sensing using speckles with fringe compensation," Opt. Express **16**, 7608-7618 (2008).

[30] A. Anand, V. K. Chhaniwal, P. Almoro, G. Pedrini, and W. Osten, "Shape and deformation measurements of 3D objects using volume speckle field and phase retrieval," Opt. Lett. **34**(10), 1522-1524 (2009).

[31] D. Axelrod. "Selective imaging of surface fluorescence with very high aperture microscope objectives," J. Biomed. Opt. **6**, 6-13 (2001).

[32] Z. Jingshan, J. Dauwels, M. Vazquez, and L. Waller, "Sparse ACEKF for phase reconstruction," Opt. Express **21**, 18125-18137 (2013).

[33] L. Waller, M. Tsang, S. Ponda, S. Y. Yang, G. Barbastathis, "Phase and amplitude imaging from noisy images by Kalman filtering," Opt. Express **19**(3), 2805-2814 (2011).

[34] Z. Jingshan, J. Dauwels, M. A. Vazquez, and L. Waller, "Efficient Gaussian inference algorithms for phase imaging," Proc. IEEE ICASSP 2012 pp. 25-30.

[35] R. Kalman, "A new approach to linear filtering and prediction problems," J. Basic Eng. **82**(1), 35-45 (1960).

[36] G. Welch and G. Bishop, An introduction to the Kalman filter, University of North Carolina at Chapel Hill, Chapel Hill, NC (1995).

[37] R. D. Niederriter, A. M. Watson, R. N. Zahreddine, C. J. Cogswell, R. H. Cormack, V. M. Bright, and J. T. Gopinath, "Electrowetting lenses for compensating phase and curvature distortion in arrayed laser systems," Applied Optics **52**, 3172 (2013).

[38] M. Herraez, D. Burton, M. Lalor, and M. Gdeisat, "Fast two-dimensional phase-unwrapping algorithm based on sorting by reliability following a noncontinuous path," Appl. Opt. **41**, 7437-7444 (2002).

[39] M. G. L. Gustafsson, "Nonlinear structured-illumination microscopy: Wide-field fluorescence imaging with theoretically unlimited resolution," Proc. Natl. Acad. Sci. USA **102**, 13081 (2005).

[40] S. W. Hell and J. Wichmann, "Breaking the diffraction resolution limit by stimulated emission: stimulated-emission-depletion fluorescence microscopy," Opt. Lett. **19**, 780-782 (1994).

[41] D. J. Stephens and V. J. Allan, "Light Microscopy Techniques for Live Cell Imaging," Science **300**, 82 (2003).

[42] D. B. Murphy, *Fundamentals of Light Microscopy and Electronic Imaging*, Wiley-Liss, New York (2001).

[43] F. Zernike, "Phase contrast, a new method for microscopic obervation of transparent objects," Physica **9**, 686-698 and 975-986, (1942).

[44] E. Cuche, P. Marquet, and C. Depeursinge, "Spatial filtering for zero-order and twin-image elimination in digital off-axis holography," Appl. Opt. **39**, 4070-4075 (2000).

[45] J. Goodman, *Introduction to Fourier Optics*, 3rd ed. (Roberts & Company Publishers, 2005).

[46] P. Gao, G. Pedrini, C. Zuo, and W. Osten, "Phase retrieval using spatially modulated illumination," Opt. Lett. **39**, 3615-3618 (2014).

[47] G. Zheng, R. Horstmeyer, and C. Yang, "Wide-field, high-resolution Fourier ptychographic microscopy," Nature Photon. **7**, 739-745 (2013).

[48] F. Zhang, G. Pedrini, and W. Osten, "Phase retrieval of arbitrary complex-valued fields through aperture-plane modulation," Phys. Rev. A **75**, 043805 (2007).

[49] P. F. Almoro, L. Waller, M. Agour, C. Falldorf, G. Pedrini, W. Osten, and S. G. Hanson, "Enhanced deterministic phase retrieval using a partially developed speckle field," Opt. Lett. **37**, 2088-2090 (2012).

[50] L. Camacho, V. Mico, Z. Zalevsky, and J. Garcia, "Quantitative phase microscopy using defocusing by means of a spatial light modulator," Opt. Express **18**, 6755-6766 (2010).

[51] J. M. Jabbour, B. H. Malik, C. Olsovsky, R. Cuenca, S. Cheng, J. A. Jo, Y-S. Cheng, J. M. Wright, and K. C. Maitland, "Optical axial scanning in confocal microscopy using an electrically tunable lens," Biomed. Opt. Express **5**, 645-652 (2014).

[52] F. O. Fahrbach, F. F. Voigt, B. Schmid, F. Helmchen, and J. Huisken, "Rapid 3D light-sheet microscopy with a tunable lens," Opt. Express **21**, 21010-21026 (2013).

[53] B. F. Grewe, F. F. Voigt, M. Hoff, and F. Helmchen, "Fast two-layer two-photon imaging of neuronal cell populations using an electrically tunable lens," Biomed. Opt. Express **2**, 2035-2046 (2011).

[54] C. Zuo, Q. Chen, W. Qu, and A. Asundi, "High-speed transport-of-intensity phase microscopy with an electrically tunable lens," Opt. Express **21**(20), 24060-24075 (2013).

[55] S. A. Alexandrov, T. R. Hillman, T. Gutzler, and D. D. Sampson, "Synthetic Aperture Fourier Holographic Optical Microscopy," Phys. Rev. Lett. **97**, 168102 (2006).

[56] S. Chowdhury and J. Izatt, "Structured illumination diffraction phase microscopy for broadband, subdiffraction resolution, quantitative phase imaging," Opt. Lett. **39**, 1015-1018 (2014).

[57] A. Faridian, D. Hopp, G. Pedrini, U. Eigenthaler, M. Hirscher, and W. Osten, "Nanoscale imaging using deep ultraviolet digital holographic microscopy," Opt. Express **18**, 14159-14164 (2010).

[58] D. J. Lee and A. M. Weiner, "Optical phase imaging using a synthetic aperture phase retrieval technique," Opt. Express **22**, 9380-9394 (2014).

[59] D. J. Lee and A. M. Weiner, "Optical Phase Imaging Using a Synthetic Aperture Phase Retrieval Technique," in CLEO: 2014, OSA Technical Digest (online) (Optical Society of America, 2014), paper JTu4A.75.

[60] P. Gao, G. Pedrini, and W. Osten, "Phase retrieval with resolution enhancement by using structured illumination," Opt. Lett. **38**, 5204-5207 (2013).

[61] Optotune Datasheet, "EL-10-30 Series," (Optotune, 2015), http://www.optotune.com/images/products/Optotune%20EL-10-30.pdf.

[62] E. Hecht, *Optics*, 4th ed. (Pearson Education, Inc., San Francisco, 2002).

[63] Z. Jingshan, R. Claus, J. Dauwels, L. Tian, and L. Waller, "Transport of intensity phase imaging by intensity spectrum fitting of exponentially spaced defocus planes," Opt. Express **22**, 10661-10674 (2014).

[64] L. Xu, X. Peng, J. Miao, and A. K. Asundi, "Studies of digital microscopic holography with applications to microstructure testing," Appl. Opt. **40**, 5046-5051 (2001).

[65] O. Matoba, T. J. Naughton, Y. Frauel, N. Bertaux, and B. Javidi, "Real-time three-dimensional object reconstruction by use of a phase-encoded digital hologram," Appl. Opt. **41**, 6187-6192 (2002).

[66] M. S. Heimbeck, M. K. Kim, D. A. Gregory, and H. O. Everitt, "Terahertz digital holography using angular spectrum and dual wavelength reconstruction methods," Opt. Express **19**, 9192-9200 (2011).

[67] A. M. Weiner, *Ultrafast Optics* (Wiley, 2009).

[68] G. Chen, C. Lin, M. Kuo, and C. Chang, "Numerical suppression of zero-order image in digital holography," Opt. Express **15**, 8851-8856 (2007).

[69] L. Ma, H. Wang, Y. Li, and H. Zhang, "Elimination of zero-order diffraction and conjugate image in off-axis digital holography," J. Mod. Opt. **56**(21), 2377-2383 (2009).

[70] N. Pavillon, C. Arfire, I. Bergond, and C. Depeursinge, "Iterative method for zero-order suppression in off-axis digital holography," Opt. Express **18**, 15318-15331 (2010).

[71] N. Pavillon, C. S. Seelamantula, J. Khn, M. Unser, and C. Depeursinge, "Suppression of the zero-order term in off-axis digital holography through nonlinear filtering," Appl. Opt. **48**, H186-H195 (2009).

[72] M. Liebling, T. Blu, and M. Unser, "Complex-wave retrieval from a single off-axis hologram," J. Opt. Soc. Am. A **21**, 367-377 (2004).

[73] K. Khare, P. T. S. Ali, and J. Joseph, "Single shot high resolution digital holography," Opt. Express **21**, 2581-2591 (2013).

[74] S. Sotthivirat and J. A. Fessler, "Penalized-likelihood image reconstruction for digital holography," J. Opt. Soc. Am. A **21**, 737-750 (2004).

[75] A. Bourquard, N. Pavillon, E. Bostan, C. Depeursinge, and M. Unser, "A practical inverse-problem approach to digital holographic reconstruction," Opt. Express **21**, 3417-3433 (2013).

[76] F. Zhao, D. C. Noll, J.-F. Nielsen, and J. A. Fessler, "Separate magnitude and phase regularization via compressed sensing," IEEE Trans. Med. Imag. **31**, 1713 -1723 (2012).

[77] K. Sauer and C. Bouman, "A local update strategy for iterative reconstruction from projections," IEEE Trans. Signal Process. **41**(2), 534-548 (1993).

[78] C. Bouman and K. Sauer, "A unified approach to statistical tomography using coordinate descent optimization," IEEE Trans. on Image Process. **5**, 480-492 (1996).

[79] C. Bouman and K. Sauer, "A generalized Gaussian image model for edge-preserving MAP estimation," IEEE Trans. on Image Process. **2**, 296-310 (1993).

[80] S. Boyd and L. Vandenberghe, *Convex Optimization* (Cambridge University Press, 2004).

[81] A. C. Kak and M. Slaney, *Principles of Computerized Tomographic Imaging* (Academic Press, New York, 1999).

APPENDIX

A. MATHEMATICAL EXPRESSIONS FOR IMPLEMENTING OPTIMIZATION IN DIGITAL HOLOGRAPHY

The optimization algorithms from Sections 4.2.4 and 4.2.5 require computation of gradients of the likelihood functions $L(\mathbf{A}, \boldsymbol{\phi})$ and $L(\mathbf{o})$. For reference, these expressions are listed below:

$$\begin{aligned}\left[\nabla_{\mathbf{A}} L(\mathbf{A}, \boldsymbol{\phi})\right]_i = 2 \left[\mathbf{A}_i^2 + \tilde{\mathbf{A}}_i^2 + 2\mathbf{A}_i\tilde{\mathbf{A}}_i \cos\left(\boldsymbol{\phi}_i - \tilde{\boldsymbol{\phi}}_i\right) - \mathbf{I}_i\right] \\ \cdot \left[2\mathbf{A}_i + 2\tilde{\mathbf{A}}_i \cos\left(\boldsymbol{\phi}_i - \tilde{\boldsymbol{\phi}}_i\right)\right],\end{aligned} \tag{A.1}$$

$$\begin{aligned}\left[\nabla_{\boldsymbol{\phi}} L(\mathbf{A}, \boldsymbol{\phi})\right]_i = -2 \left[\mathbf{A}_i^2 + \tilde{\mathbf{A}}_i^2 + 2\mathbf{A}_i\tilde{\mathbf{A}}_i \cos\left(\boldsymbol{\phi}_i - \tilde{\boldsymbol{\phi}}_i\right) - \mathbf{I}_i\right] \\ \cdot \left[2\mathbf{A}_i\tilde{\mathbf{A}}_i \sin\left(\boldsymbol{\phi}_i - \tilde{\boldsymbol{\phi}}_i\right)\right],\end{aligned} \tag{A.2}$$

$$\left[\nabla_{\mathbf{o}} L(\mathbf{o})\right]_i = 2 \left[|\mathbf{r}_i|^2 + |\mathbf{o}_i|^2 + \mathbf{o}_i\mathbf{r}_i^* + \mathbf{o}_i^*\mathbf{r}_i - \mathbf{I}_i\right] \cdot \left[\mathbf{o}_i^* + \mathbf{r}_i^*\right]. \tag{A.3}$$

VITA

VITA

Dennis J. Lee received his B.S. and M.S. degrees in Electrical and Computer Engineering from Purdue University, West Lafayette, IN, USA in 2009 and 2013, respectively. Dennis is currently a Ph.D. candidate in the School of Electrical and Computer Engineering at Purdue University. His research focus is computational imaging, which aims to integrate image processing algorithms with novel ways of taking measurements. Related areas include microscopy, optics, digital signal processing, image reconstruction, and imaging systems. During his graduate career, he has taught a weekend science enrichment class for students in third and fourth grades. He has received the Charles C. Chappelle Fellowship in 2010, the Mary Williams Estate Fellowship in 2011, and the Fittante Fellowship in 2012 from the Purdue University Graduate School and the Purdue University School of Electrical and Computer Engineering for academic excellence.